

CURE: Curriculum-guided Multi-task Training for Reliable Anatomy Grounded Report Generation

Pablo Messina^{1,2,3}, Andrés Villa⁴, Juan León Alcázar⁴, Karen Sánchez⁴,

Carlos Hinojosa⁴, Denis Parra^{1,2,3}, Alvaro Soto^{1,2}, Bernard Ghanem⁴

¹Pontificia Universidad Católica de Chile, ²CENIA, ³iHEALTH, ⁴KAUST

pamessina@uc.cl, {andres.villa, juancarlo.alcazar, karen.sanchez, carlos.hinojosa}@kaust.edu.sa
 {dparra, asoto}@ing.puc.cl, bernard.ghanem@kaust.edu.sa

Abstract

Medical vision–language models can automate the generation of radiology reports but struggle with accurate visual grounding and factual consistency. Existing models often misalign textual findings with visual evidence, leading to unreliable or weakly grounded predictions. We present “CURE”, an error-aware curriculum learning framework that improves grounding and report quality without any additional data. CURE tunes a multi-modal instructional model on phrase grounding, grounded report generation, and anatomy-grounded report generation using public datasets. The method dynamically adjusts sampling based on model performance emphasizing harder samples to improve spatial and textual alignment. CURE improves grounding accuracy by +0.37 IoU, boosts report quality by +0.188 CXRFEScore, and reduces hallucinations by 18.6%. CURE is a data-efficient framework that enhances both grounding accuracy and report reliability. Code is available at <https://github.com/PabloMessina/CURE> and model weights at <https://huggingface.co/pamessina/medgemma-4bit-cure>.

1. Introduction

In the medical domain, Vision-language Models (VLMs) enable the automatic generation of diagnostic reports from imaging exams, thereby reducing the workload of specialists and promoting standardized diagnostic pipelines [3, 23, 38]. Despite their remarkable success in bridging visual and textual modalities [1, 10, 25, 35, 46], VLMs still face fundamental challenges when applied to specialized domains such as medicine. The factuality and reliability of VLMs remain a significant concern, as current architectures often generate outputs that are inconsistent with their visual input, a phenomenon known as hallucinations [24, 45, 48].

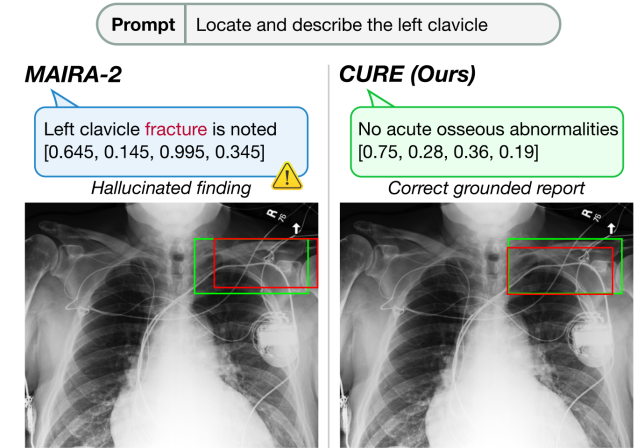


Figure 1. **False Positive Detection of Pathologies.** Given the same chest X-ray input both models approximate the location of the left clavicle. However, the baseline model (MAIRA-2) hallucinates a fracture (there is no fracture in the image), whereas our proposed model (CURE) generates a clinically correct and visually grounded description.

Medical VLMs [23, 38, 55] rely on large-scale, domain-specific datasets to adapt general-purpose multi-modal models for medical applications. While this standard fine-tuning strategy improves performance on medical benchmarks, the resulting models often lack visual grounding, thus limiting interpretability and increasing the risk of hallucinations [47]. For clinical adoption, it is crucial that VLMs produce factually accurate outputs and correctly ground medical findings in the relevant image regions. Strengthening factuality and grounding is therefore essential to ensure transparency, trustworthiness, and the reliable deployment of medical VLMs in real-world workflows.

To address these drawbacks, state-of-the-art models such as MAIRA-2 [3] explicitly incorporate grounded report generation to better align local visual evidence with the textual findings. For example, MAIRA-2 is trained on a diverse

set of localization-based tasks, including phrase grounding and grounded report generation. However, as shown in Figure 1, current models often exhibit a bias in which the target visual regions become overly associated with abnormal findings, leading to false positives in medical reports.

To address these limitations, we propose **CURE** (**C**URriculum-guided **M**ulti-task **T**raining for **R**Eliable **A**natomy **G**rounded **R**eport **G**eneration), a curriculum-based learning framework that enhances the reliability and visual grounding of medical VLMs without requiring additional data. CURE improves the standard training pipeline, and obtains improved results using only a subset of publicly available chest X-ray datasets. In particular, CURE replaces the conventional finding-generation objective used in state-of-the-art methods with an anatomy-grounded report generation (AGR) task, thus leveraging the most detailed regional annotations provided by some datasets.

Our contributions are threefold: **i**) We introduce CURE, a novel error-aware curriculum framework that dynamically adjusts sampling distributions based on model performance, enhancing visual grounding without requiring any additional training data. **ii**) Our training strategy enables the effective transfer of grounding capabilities to medical VLMs that originally lack visual grounding mechanisms. These models surpass the current state of the art in visual grounding, despite being trained on less training data. **iii**) On the Chest Imagenet dataset, CURE achieves an 18.6% reduction in hallucinations across six key anatomical regions, substantially improving the reliability and trustworthiness of medical VLM outputs and setting a new state-of-the-art in visually grounded report generation.

2. Related Work

Medical Vision-language Models. The adoption of Vision-language models (VLMs) in the medical domain has advanced rapidly in recent years [15, 18, 31, 42]. Early approaches primarily targeted clinical report generation and captioning tasks, while more recent models such as Med-PaLM [42, 43], MAIRA-2 [2], and the recently released MedGemma [39] exhibit strong multi-modal reasoning capabilities across diverse medical modalities. Despite their success, the challenge of efficiently fine-tuning these large models on heterogeneous and task-specific medical datasets remains largely unsolved. Our work builds upon this line of research by introducing a structured, error-aware training curriculum that enhances performance without requiring additional data or model parameters.

Multi-Task Learning in Medical Imaging. Multi-task learning (MTL) is a widely adopted paradigm for jointly training models on related objectives such as classification, segmentation, and report generation [8, 26, 56]. In medical imaging, MTL has been successfully applied across modalities, improving both efficiency and generalization [6, 9, 20,

30, 36, 50, 51]. For instance, Sainz *et al.* [36] leveraged MTL for breast cancer screening by jointly learning classification and detection of abnormal findings in mammography; Chen *et al.* [9] improved atrial segmentation and classification using MRI; and Weninger *et al.* [50] enhanced brain tumor segmentation by coupling detection and image reconstruction tasks in brain MRI. Despite these advances, MTL performance strongly depends on how task contributions are balanced during training [19]. Improper weighting can cause task dominance and negative transfer [30, 40, 54], degrading overall performance. To address this limitation, we propose an adaptive curriculum that dynamically schedules data exposure based on model performance, allowing the network to automatically prioritize under-performing tasks rather than relying on manually tuned loss weights.

Curriculum Learning. Curriculum learning (CL)[4, 49] trains models by gradually increasing task difficulty, starting from easier samples and progressing to harder ones, in analogy to human learning. CL has been successfully applied to medical imaging [22, 41]. For instance, Shibu *et al.* [41] introduced a MedSAM-guided CL strategy for white matter tract segmentation, where the curriculum is defined by anatomical block complexity to progressively refine spatial representations. Similarly, Li *et al.* [22] introduced a dynamic CL framework for medical image classification that derives sample difficulty from in-domain uncertainty estimates (via a Dirichlet classifier) and adapts the sampling schedule accordingly. Most CL implementations rely on predefined or heuristic difficulty measures. Instead, more recent extensions, termed self-paced learning (SPL) [21], estimate sample difficulty using the training loss at each iteration. Yet, SPL tends to repeatedly select easy samples, since data points with lower losses are consistently prioritized. To overcome this limitation, Jiang *et al.* [16] proposed self-paced curriculum learning (SPCL), which integrates prior knowledge from predefined curricula with the adaptive nature of SPL, enabling the model to leverage both task structure and feedback during learning. Building on this principle, our method employs an error-aware sampling strategy, where sample difficulty is inferred from the model’s current error distribution across tasks and data subsets. Unlike prior work, our curriculum integrates both spatial and textual feedback to guide training in grounded medical vision-language models.

3. Methodology

Our curriculum-guided multi-task training framework, CURE, enhances the capabilities of medical VLMs by reformulating the training methodology without requiring additional data. CURE restructures existing datasets into a unified, fine-grained instructional format. In addition, it introduces an error-aware curriculum that dynamically adjusts sampling based on the model’s performance across

Table 1. **Dataset composition and statistics.** Number of instances for each task across the training, validation, and test splits. The MIMIC-CXR dataset serves as a superset, providing the Chest ImaGenome (CIG) and MS-CXR subsets for training and its official test split for report-generation evaluation. Evaluation-only datasets are used to assess generalization performance. **AGR** refers to Anatomy Grounded Report Generation, **PG** to Phrase Grounding, and **GRG** to Grounded Report Generation.

Dataset	Task	# Train	# Val	# Test
Training & In-Domain Evaluation				
MIMIC-CXR (CIG)	AGR Locate	8.5M‡	69.9K†	
MIMIC-CXR (CIG)	AGR Describe	2.3M‡	18.8K†	1,000*
MIMIC-CXR (CIG)	AGR Loc., Desc.	2.1M‡	17.4K†	
MIMIC-CXR (MS-CXR) PG		815‡	169†	176
MIMIC-CXR (Test Split) Report Generation		—	—	3,155
PadChest-GR	GRG	3,185‡	455†	915
PadChest-GR	PG	8,871***‡	1,297†***	1,238
Zero-Shot Generalization				
VinDr-CXR	GRG	—	—	3,000
VinDr-CXR	PG	—	—	2,108

*A sampled subset of 1,000 from 123,319 total available instances.

**Includes both original report phrases and fine-grained labels as phrases.

†Each curriculum cycle evaluates a stratified random subset of the validation set.

‡Due to computational constraints, only a fraction of the total available instances are used. With 9,000 training steps and an effective batch size of 25, a maximum of 225,000 instances ($\approx 1.74\%$ of the total) are processed.

datasets and anatomical categories. This reformulated training pipeline enables the model to focus on challenging samples and underperforming regions progressively.

3.1. Error-Aware Curriculum Learning

Our training setup involves a collection of k distinct data sources, $\mathcal{D} = \{D_1, D_2, \dots, D_k\}$. Each data source (D_i) corresponds to a specific dataset and its original supervision task, such as phrase grounding (PG) in MS-CXR or anatomy grounded report generation (AGR) in Chest ImaGenome. Under standard multi-task training, samples are drawn from \mathcal{D} in proportion to the dataset size ($|D_i|$), the sampling probability for D_i is defined as: $p_i = |D_i|/|\mathcal{D}|$.

However, medical imaging datasets are inherently imbalanced in terms of relative dataset sizes and in the distribution of anatomical or semantic classes within each dataset. The second source of imbalance is further emphasized due to variations in patient demographics, acquisition protocols, and the natural frequency of clinical conditions [37].

As shown in Table 1, our data composition reflects this imbalance: over 12.9M instances from Chest ImaGenome dominate the much smaller MS-CXR (815 PG instances) and PadChest-GR ($\sim 12k$ instances) datasets. Beyond the imbalance between datasets, each dataset also exhibits substantial intra-dataset class imbalance. For example, anatomical regions in AGRG and semantic categories in PG are

unevenly represented, leading the model to overfit frequent regions, neglect rare but clinically important ones, and hallucinate findings (Figure 1). Our curriculum framework addresses both sources of imbalance.

To mitigate these issues, we introduce an error-aware curriculum learning strategy [13] that dynamically adjusts sampling probabilities at two levels of granularity: (i) at the dataset level, where we re-weight the relative number of training samples per dataset, and (ii) at the class level, where we re-weight samples per anatomical region or semantic class. The curriculum proceeds over n iterative stages. Each stage consists of three steps: training, evaluation, and sample re-weighting. The sampling probability for each data source (p_i) and class is modulated by the error rate (e_i) at the current stage. The sampling probabilities estimated at stage n are used to initialize stage $n + 1$, while the first stage starts with a uniform distribution *i.e.*, $p_i = p_j$ for all i, j . The overall procedure is illustrated in Figure 2.

Data Source Evaluation. To maintain computational efficiency, each stage evaluates a random, fixed-size subset from each validation source (e.g., ~ 200 samples for Chest ImaGenome, ~ 150 for PadChest-GR, and ~ 100 for MS-CXR). For each subset, we assess boxes localization quality using Intersection over Union (IoU) and textual fidelity using CXRFEScore [29], which captures clinical semantic similarity. These metrics determine the updated sampling weights for the next stage.

Inter-Dataset Curriculum. After each evaluation stage, we compute an aggregate performance score (s_i) for each data source D_i as a weighted sum of the two metrics:

$$s_i = \alpha \cdot \text{IoU}_i + (1 - \alpha) \cdot \text{CXRFEScore}_i, \quad (1)$$

where α controls the trade-off between localization accuracy and semantic quality. The error for each source is defined as $e_i = 1 - s_i$. The sampling probability for the next training stage is then obtained by normalizing these errors:

$$p_i = \frac{e_i}{\sum_{j=1}^K e_j}. \quad (2)$$

Intra-Dataset Curriculum. Within each dataset, the curriculum operates at a finer granularity by re-weighting categories, anatomical regions, or semantic groups based on their per-class error. For phrase grounding (PG) in MS-CXR [5], we group samples by the eight original phrase classes (e.g., pneumonia, consolidation). In PadChest-GR [11], where annotations span 155 labels organized into 26 higher-level label groups (e.g., atelectasis, cardiomegaly), we apply the curriculum at the group level.

The most fine-grained application of the curriculum occurs in Chest ImaGenome [53] for the anatomy grounded report generation (AGR) task. AGRG comprises three subtasks: *Locate*, *Describe*, and *Locate and describe*, sampled uniformly to preserve task balance. The curriculum

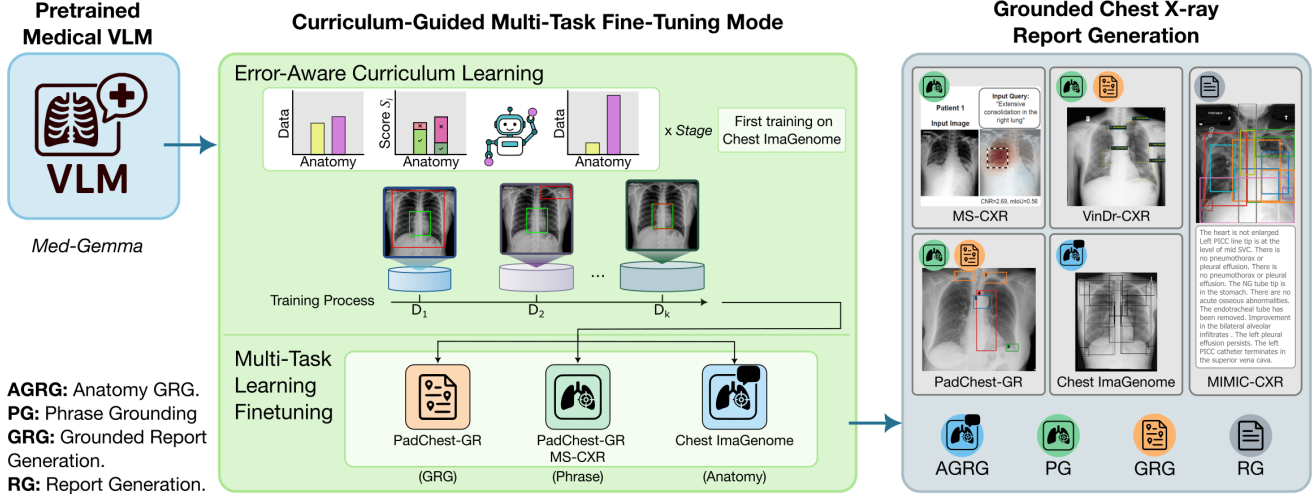


Figure 2. Overview of CURE, our Curriculum-guided Multi-task Training Framework. During training, the model is periodically evaluated every N steps on validation subsets from each task. Performance metrics (IoU, CXRFEScore) are calculated to identify task-level and category-level errors, which are then used to update the sampling weights in the training sampler. The cycle then resumes, allowing the model to focus more heavily on the data it finds most challenging. Evaluation of the RG task uses the official MIMIC-CXR test set, while VinDr-CXR is assessed in a zero-shot setting.

acts within each subtask by re-weighting anatomical locations according to their error.

Because annotation coverage differs across subtasks, each one has its own set of available locations (i.e., 36 with bounding box for *Locate*, 38 with text for *Describe*, and 29 with both annotations for *Locate and describe*). This formulation allows the model to focus on anatomical regions that are spatially or semantically challenging, improving both localization and descriptive quality.

For the grounded report generation (GRG) task in PadChest-GR, we do not apply intra-dataset re-weighting. These reports contain multiple co-occurring findings spanning several anatomical and pathological categories. Since there is no straightforward or well-defined way to categorize such multi-label instances for fine-grained rebalancing, we adopt uniform sampling for this task.

3.2. Fine-Grained Task Formulation

CURE re-formulates diverse tasks into a unified, fine-grained instructional format. Each training instance from the source dataset D_i is represented as a triplet (*image*, *instruction*, *response*), allowing heterogeneous supervision (bounding boxes, phrases, anatomical labels, and descriptive sentences) to be learned under a consistent multi-task framework.

Phrase Grounding (PG). For MS-CXR and PadChest-GR, the original annotations link phrases within a report to one or more corresponding bounding boxes on the image. We transform these annotations into direct grounding instructions. For each annotated phrase, we create a sample using the template prompt *Ground the phrase:*

{phrase}. When a phrase is associated with multiple bounding boxes, all of them are included in the response. The expected output is the phrase followed by one or more normalized bounding box coordinates: *phrase: [cx₁, cy₁, w₁, h₁] ... [cx_n, cy_n, w_n, h_n]*.

PadChest-GR provides 8,489 sentences and 155 unique, fine-grained clinical labels. To enrich our training data, we exploit this dual annotation by generating additional instances: for each (*sentence*, *box list*) pair, we create (*label*, *box list*) pairs. For example, from “Minimal biapical pleural thickening” with label “apical pleural thickening” and bounding box [cx, cy, w, h], we produce one instance for the sentence and another for the label. This augmentation, applied only to training and validation splits, nearly doubles the PadChest-GR PG data and helps the model ground natural descriptions and canonical clinical terms. The test set remains un-augmented.

Grounded Report Generation (GRG). In the PadChest-GR’s GRG task, the model must produce a complete report in which grounded findings are explicitly linked to bounding boxes. We use the instruction: *Generate a grounded report.* The target response is the ground-truth report, where phrases corresponding to available bounding box annotations are augmented with their coordinates directly in the text. For example, an output may take the form: {phrase₁} [cx₁, cy₁, w₁, h₁]. {phrase₂} [cx₂, cy₂, w₂, h₂], where each phrase is linked to its corresponding list of bounding boxes.

Anatomy-Grounded Report Generation (AGRG). Chest Imagenome provides detailed scene-graphs linking anatomical locations in MIMIC-CXR frontal-view images

Table 2. **Results for Phrase Grounding (PG).** We report Micro-Average IoU (IoU Mi. \uparrow) and Macro-Average IoU (IoU Ma. \uparrow) on three test sets: MS-CXR, PadChest-GR, and zero-shot VinDr-CXR. CURE consistently improves localization performance across all metrics and datasets, including VinDr-CXR, which was not seen during training.

Model	MS-CXR		PadChest-GR		VinDr-CXR (Zero-Shot)	
	IoU Mi. \uparrow	IoU Ma. \uparrow	IoU Mi. \uparrow	IoU Ma. \uparrow	IoU Mi. \uparrow	IoU Ma. \uparrow
MAIRA-2	0.496	0.452	0.280	0.287	0.162	0.115
CURE	0.554	0.495	0.453	0.438	0.244	0.205

to both descriptive sentences and bounding boxes. This detailed structure is ideal for our AGRG fine-grained task decomposition as it allows for a significant expansion of the training data: a single image can yield multiple training instances, one for each annotated location. Concretely, the $\sim 237k$ images in the training split generate an average of 9 to 36 instructional instances per image, depending on the subtask, culminating in millions of viable training samples reported in Table 1. From this large pool, we create three distinct subtasks:

- **Locate:** To train pure spatial localization, we use the prompt `Locate the {location}`. The expected output follows the format: `Location of the {location}: [cx, cy, w, h]`.
- **Describe:** To train contextual description independent of localization, we use the prompt `Describe the {location}`. The target output is formatted as: `Description of the {location}: {description}`.
- **Locate and Describe:** To train the model to perform both tasks simultaneously, we prompt: `Locate and describe the {location}`. The response combines both formats: `Location of the {location}: [cx, cy, w, h]. Description: {description}`.

This multi-prompt formulation explicitly disentangles and teaches the model the diverse tasks of localization and description. This process generates over 12.9M potential training instances, it is important to note that due to computational constraints, only a fraction of this pool is sampled during training, as detailed in the footnote of Table 1.

4. Experiments

We present a comprehensive empirical evaluation of CURE across three tasks: Anatomy-Grounded Report Generation, Grounded Report Generation, and Phrase Grounding. In addition, we validate on the traditional report generation (RG) task by repurposing the AGRG and GRG setups for fair comparison. We benchmark CURE against state-of-the-art methods and conduct an ablation study to analyze the con-

tributions of its core components, evaluating the impact of each design choice on our two main metrics: grounding accuracy (IoU) and report quality (CXRFEScore).

Datasets. CURE adopts a multi-task fine-tuning strategy on the same three publicly available chest X-ray datasets used by our baseline (MAIRA-2), enabling a fair and comparable evaluation. Chest Imagenome [53] provides scene graphs linking anatomical regions to bounding boxes and report sentences, and is used for the Anatomy-Grounded Report Generation task. PadChest-GR [11] contains radiology reports with phrases explicitly grounded to bounding boxes, supporting both Grounded Report Generation and Phrase Grounding tasks. MS-CXR [5] is a smaller dataset derived from MIMIC-CXR [17], providing bounding box annotations for report phrases, and is used exclusively for Phrase Grounding. For zero-shot evaluation, we also include VinDr-CXR [32], using its official test split to assess the model’s generalization to unseen data distributions.

Evaluation Metrics. For the *Grounded Report Generation* task, localization performance is measured using the mean Intersection over Union (IoU), while textual report quality is evaluated using CheXbert [44] metrics (such as Precision, Recall, F1-score, and Cosine Similarity), CXRFEScore [28], and RadGraph F1 [12]. For the *Phrase Grounding task*, we report both micro- and macro-averaged IoU to evaluate across and within categories. Please refer to our supplementary material for a detailed overview of the tasks, corresponding prompt formats, and expected output structures for each dataset used in our experiments.

We use MedGemma-4B-IT [38] as the base model, fine-tuned with LoRA [14] at rank 16 in 4-bit precision. All training stages use the AdamW optimizer [27] with a consistent set of hyperparameters: an effective batch size of 25 (per-device batch size 5 with 5 gradient accumulation steps), a learning rate of 2×10^{-4} , a linear scheduler with a 0.03 warmup ratio, and gradient clipping with maximum gradient norm set to 0.3. Optimizer and scheduler states are not carried over between phases. The initial 3000-step pre-training has its own optimizer instance, and a new one is initialized for the subsequent 6000-step multi-task phase, preserving only the model weights. Data augmentation includes spatial transformations and contrast-limited adaptive histogram equalization (CLAHE) [58].

Baseline Methods. We compare CURE against two strong baselines. First, we evaluate MedGemma-4B-IT [38] to establish the pretrained model’s baseline performance. Second, we include MAIRA-2 [2], a state-of-the-art open-source medical vision-language model that jointly learns grounding and report generation tasks.

4.1. Comparison against State-of-the-Art

Visual Grounding. Table 2 shows that CURE consistently outperforms MAIRA-2 across all metrics (Micro and Macro

IoU) and datasets, including MS-CXR and PadChest-GR. CURE achieves larger relative gains on PadChest-GR than on MS-CXR, highlighting the effectiveness of the proposed error-aware reweighting strategy.

Anatomy-Grounded Report Generation. For Chest ImaGenome, CURE attains a +0.37 IoU improvement over MAIRA-2, more than doubling its localization performance (see Table 3). We note that CURE’s base model (MedGemma-4B-IT) lacks visual grounding capabilities, therefore, these results demonstrate that CURE training pipeline successfully transfers and enhances the grounding ability. This result is particularly noteworthy as CURE also surpasses MAIRA-2’s IoU on the Grounded Report Generation task (Table 4), even though MAIRA-2 benefits from pretraining on the large proprietary USMix dataset [3] containing 193,652 text-only reports and over 69,043 grounded reports to which we do not have access.

Report Generation Performance. We evaluate CURE across three report generation tasks: on the MIMIC-CXR test set for standard report generation, and on Chest ImaGenome and PadChest-GR for the AGRG and GRG tasks, respectively. Table 3 presents AGRG results on a 1,000 sample subset of the Chest ImaGenome test set (see Table 1). While our model’s most significant improvement is in spatial grounding, it also shows enhanced performance in most text-based metrics for this fine-grained, in-domain task. CURE achieves the highest scores on F1-Mi (0.474), cosine similarity (0.649), and CXRFEScore (0.548), outperforming the baseline models.

Table 4 reports GRG performance on PadChest-GR. This task naturally favors MAIRA-2, owing to its additional training on the proprietary USMix dataset, which allows it to surpass CURE on most text-based metrics. In contrast, CURE consistently delivers higher grounding accuracy, achieving the best mean IoU (0.265). Although CURE does not outperform MAIRA-2 on text-based metrics, it substantially boosts MedGemma-4b-IT’s performance in these metrics. This highlights the effectiveness of our training paradigm, particularly given that PadChest-GR (GRG) contains far fewer training instances than its version for PG and Chest ImaGenome for AGRG.

Table 3. Results for Anatomy-Grounded Report Generation (AGRG) on Chest ImaGenome (CIG). We report mean IoU (\uparrow), CheXbert F1 (micro/macro) (\uparrow), CheXbert cosine similarity (\uparrow), and CXRFEScore (\uparrow). **Bold** values indicate the best performance for each metric.

Model	IoU \uparrow	F1-Mi \uparrow	F1-Ma \uparrow	Cos. \uparrow	CXRFEScore \uparrow
MAIRA-2	0.226	0.272	0.100	0.557	0.360
MedGemma-4B-IT	–	0.344	0.294	0.631	0.477
CURE	0.596	0.474	0.273	0.649	0.548

Table 5 shows performance on the MIMIC-CXR test set, comprising 3,155 frontal views. For fair comparison, all models generate reports from the same frontal view. Our CURE (AGRG) variant, generates reports by concatenating the descriptions for 29 distinct anatomical locations, outperforms all the baselines in recall scores (R-Ma: 0.540, R-Mi: 0.749), and the combined CURE (AGRG+GRG) further improves this (R-Ma: 0.582, R-Mi: 0.781), demonstrating that our fine-grained approach effectively captures a wide range of findings. The top-performing model on most metrics is CXRMate-RRG24 [33], the winner of a recent radiology report generation competition. Its leading RadGraph F1 score is consistent with its training, which was optimized via reinforcement learning using RadGraph F1 as a reward. Comparatively, our model remains competitive on semantic similarity metrics, achieving the highest CheXbert Cosine Similarity (0.792) and a close second on CXRFEScore (0.655). CURE also achieves the highest CheXbert F1 macro (0.415).

Evaluating Hallucination and Reliability. To complement our empirical evaluation, we conduct a targeted analysis of hallucination and report consistency on the AGRG task. The evaluation is performed on a subset of the Chest ImaGenome test set, comprising 300 examples for six key anatomical locations (1800 images in total). We prompted CURE using its `Locate` and `describe` instruction and prompted MAIRA-2 to ground and describe the same location. We then employed Gemini 2.5 Flash Lite to perform a Natural Language Inference (NLI) comparison between each model’s generated description for a specific anatomy and the full ground-truth MIMIC-CXR report.

The results, detailed in Table 6, show that CURE offers a substantial improvement in reliability. On average, CURE reduces the hallucination rate of abnormal findings to 8.78% from MAIRA-2’s 26.50%. It also cuts the contradiction rate in half (17.44% vs. 33.22%) and more than doubles the entailment rate (39.50% vs. 15.94%). The improvement is particularly stark for bone structures like the clavicles, where CURE’s hallucination rate is only 1.00% compared to MAIRA-2’s rates of over 59%.

While MAIRA-2 exhibits a slightly lower hallucination rate for a few anatomies (e.g., ‘Cardiac Silhouette’), CURE consistently achieves a significantly lower contradiction rate and higher entailment rate across almost all categories. This improved performance likely stems from a key difference in the training data composition. Standard phrase grounding, used by MAIRA-2, is inherently biased towards abnormal findings. In contrast, our AGRG formulation exposes the model to both normal and abnormal descriptions for each anatomical region, leading to a more balanced and reliable generative process that mitigates the tendency to hallucinate abnormalities.

Zero-Shot Performance. To assess the generalization ca-

Table 4. **Results for Grounded Report Generation (GRG) on PadChest-GR and zero-shot VinDr-CXR.** We report mean IoU (↑), CheXbert F1 (micro/macro) (↑), CheXbert cosine similarity (↑), and CXRFEScore (↑). Bold values indicate the best score for each metric.

Model	PadChest-GR					VinDr-CXR (Zero-Shot)				
	IoU ↑	F1-Mi ↑	F1-Ma ↑	Cos. ↑	CXRFEScore ↑	IoU ↑	F1-Mi ↑	F1-Ma ↑	Cos. ↑	CXRFEScore ↑
MAIRA-2	0.256	0.592	0.325	0.844	0.616	0.216	0.546	0.237	0.824	0.592
MedGemma-4B-IT	–	0.144	0.198	0.733	0.517	–	0.209	0.196	0.779	0.596
CURE	0.265	0.507	0.271	0.819	0.574	0.262	0.505	0.229	0.832	0.540

Table 5. **Results for Report Generation (RG) on the MIMIC-CXR test set.** We report CheXbert F1 (F1-Ma/Mi) (↑), Precision (P-Ma/Mi) (↑), and Recall (R-Ma/Mi) (↑), each macro (Ma) and micro (Mi) averaged together with CheXbert, Cosine Similarity (Cos.) (↑), CXRFEScore (CXRFES) (↑), and RadGraph F1 (RadF1) (↑). **Bold** and underlined values indicate the best and second-best models per metric, respectively.

Model	F1-Ma ↑	F1-Mi ↑	P-Ma ↑	P-Mi ↑	R-Ma ↑	R-Mi ↑	Cos. ↑	CXRFEScore ↑	RadF1 ↑
CXRMate-RRG24	<u>0.414</u>	0.589	0.493	<u>0.617</u>	0.415	0.563	0.764	0.656	0.255
MAIRA-2 (w/ grounding)	0.304	0.490	<u>0.442</u>	0.639	0.283	0.397	0.751	0.603	0.120
MAIRA-2 (w/o grounding)	0.386	0.555	0.425	0.578	0.385	0.534	0.693	0.576	0.143
MedGemma-4B-IT	0.382	0.547	0.332	0.452	0.494	0.692	0.714	0.580	0.112
CURE (GRG)	0.314	0.464	<u>0.442</u>	0.606	0.290	0.376	0.725	0.526	0.077
CURE (AGRG)	0.400	0.559	0.355	0.446	<u>0.540</u>	<u>0.749</u>	<u>0.783</u>	0.645	<u>0.181</u>
CURE (AGRG+GRG)	0.415	<u>0.562</u>	0.365	0.439	0.582	0.781	0.792	<u>0.655</u>	0.176

pabilities of CURE beyond the datasets seen during training, we further evaluate the model on the VinDr-CXR test split for both PG and GRG (see Tables 2 and 4). As shown in Table 2, CURE surpasses MAIRA-2 in grounding performance on the PG task, achieving higher Micro and Macro IoU. Similarly, on the GRG task, CURE equips MedGemma-4B-IT with a strong grounding ability, outper-

forming MAIRA-2 in IoU and narrowing the gap in text-based metrics, despite MAIRA-2’s advantage from training on proprietary GRG-specific data. These results demonstrate that the capabilities learned through CURE generalize effectively to out-of-domain datasets and task formats.

4.2. Ablation Study

To assess the contribution of each component in our training pipeline, we conduct a detailed ablation study summarized in Table 7. For context, we include MAIRA-2 as a strong external baseline. Our analysis begins with a multi-task fine-tuned baseline (v1), trained without data augmentation, curriculum learning, or specialized pre-training.

Even this simplest variant already surpasses MAIRA-2 on the AGRG task and on the zero-shot VinDr-CXR PG task, highlighting the effectiveness of our fine-grained task reformulation. However, v1 underperforms on GRG IoU and on the MS-CXR PG task. Adding **data augmentation** (v2) yields small but consistent improvements in PG performance across all three grounding datasets.

We then examine the effect of **curriculum learning** by varying the frequency of our performance-based reweighting strategy (v3–v5). A reweighting interval of 3000 steps (v5) produces the most stable and substantial gains, outperforming both more frequent and less frequent updates. We therefore adopt this interval in all subsequent experiments.

A larger gain emerges when introducing a dedicated **Chest ImaGenome pre-training stage** (v6–v8). Increasing the pre-training duration to 3000 steps (v8) enables the model to exceed MAIRA-2 on the MS-CXR PG task (0.497 vs. 0.496), emphasizing the value of grounding-specific

Table 6. **Hallucination analysis for AGRG on a Chest ImaGenome subset.** We report abnormal finding hallucination rates (%) and assess report consistency using a Natural Language Inference (NLI) framework, reporting the fraction (%) of Contradiction (Cont.) and Entailment (Entail). Lower hallucination and contradiction rates, together with higher entailment rates, indicate better clinical faithfulness and grounding quality.

Model	Anatomy	Abn. ↓	Cont. ↓	Entail. ↑
MAIRA-2	Cardiac Silhouette	2.00	8.00	25.00
CURE	Cardiac Silhouette	25.67	27.67	47.33
MAIRA-2	Left Clavicle	59.00	22.67	5.00
CURE	Left Clavicle	1.00	7.00	32.67
MAIRA-2	Left Lung	12.00	56.33	21.67
CURE	Left Lung	7.00	32.33	41.67
MAIRA-2	Right Clavicle	62.67	20.33	1.67
CURE	Right Clavicle	1.00	7.33	27.67
MAIRA-2	Right Lung	10.67	53.67	29.33
CURE	Right Lung	11.67	27.00	46.00
MAIRA-2	Spine	12.67	38.33	13.00
CURE	Spine	6.33	3.33	41.67
MAIRA-2	Mean Anatomies	26.50	33.22	15.94
CURE	Mean Anatomies	8.78	17.44	39.50

Table 7. **Ablation Study.** We evaluate the contribution of each component across three grounding tasks. CXRS denotes the CXRFEScore metric. For Phrase Grounding (PG), we report Micro-Averaged IoU on MS-CXR (MS), PadChest-GR (PC), and VinDr-CXR (VD). Note that: CL(f) indicates curriculum learning with a reweighting frequency of f steps, CIG(s) denotes a Chest Imagenet pre-training stage of s steps, HPS refers to hyperparameter search. Best value for each metric is shown in **bold**.

Model Configuration	AGR (CIG)		GR (PC)		PG (IoU Mi. ↑)		
	IoU ↑	CXRS ↑	IoU ↑	CXRS ↑	MS	PC	VD
MAIRA-2 (External Baseline)	0.226	0.360	0.256	0.616	0.496	0.280	0.162
v1: Base (w/o Aug, w/o CL, w/o CIG)	0.393	0.565	0.171	0.589	0.389	0.356	0.192
v2: + Aug	0.378	0.552	0.185	0.602	0.406	0.365	0.205
v3: + Aug + CL(1.5k)	0.402	0.556	0.179	0.592	0.410	0.383	0.211
v4: + Aug + CL(2k)	0.394	0.542	0.193	0.596	0.395	0.383	0.197
v5: + Aug + CL(3k)	0.419	0.552	0.180	0.596	0.432	0.393	0.205
v6: + Aug + CIG(1k) + CL(3k)	0.452	0.544	0.195	0.591	0.459	0.395	0.220
v7: + Aug + CIG(2k) + CL(3k)	0.444	0.525	0.203	0.587	0.468	0.404	0.223
v8: + Aug + CIG(3k) + CL(3k)	0.469	0.546	0.206	0.582	0.497	0.422	0.225
v9 (CURE): + Aug + CIG(3k) + CL(3k) + HPS	0.596	0.548	0.265	0.574	0.554	0.453	0.244

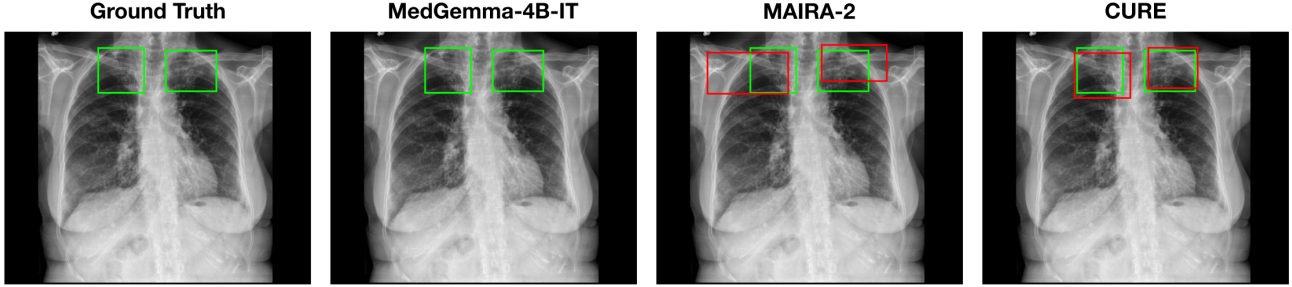


Figure 3. **Qualitative Results.** Qualitative phrase grounding (PG) results for the prompt “*Chronic inflammatory changes predominantly in both lung apices*,” shown on an example from the PadChest-GR dataset [11]. Ground-truth regions are shown in green across all images for reference. Model predictions from **CURE** and **MAIRA-2** are shown in red. The **MedGemma-4B-IT** model does not output visual grounding and therefore displays no predicted regions.

pre-training before the curriculum stage.

Finally, we perform an extensive hyperparameter search (HPS) for both the pre-training stage and the multi-task fine-tuning phase (v9). Our final model, **CURE** (v9), achieves the best overall performance, notably surpassing MAIRA-2 on the challenging GRG IoU benchmark (0.265 vs. 0.256), while maintaining strong results across all other tasks.

4.3. Qualitative Analysis

Figure 3 shows phrase grounding results for the phrase “*Chronic inflammatory changes predominantly in both lung apices*” on an image from PadChest-GR [11]. Both CURE and MAIRA-2 successfully identify the lung apices associated with the described findings. However, CURE’s localization is more accurate and better aligned with the phrase semantics, while MAIRA-2 provides a coarser prediction that only partially covers the relevant areas. As expected, MedGemma-4B-IT does not produce visual grounding outputs, and thus no bounding boxes are shown for this model.

5. Conclusion

We introduced CURE, an error-aware curriculum learning framework that advances visual grounding and factual reliability in medical vision–language models through adaptive multi-task training on existing public datasets. By dynamically prioritizing underperforming samples and categories, CURE delivers consistent improvements over the baseline across diverse tasks, including phrase grounding, where it outperforms in all Micro and Macro IoU metrics on datasets such as MS-CXR, PadChest-GR, and VinDr-CXR. Moreover, CURE enables effective grounding in the base MedGemma-4B-IT model—which originally lacks visual grounding capabilities—achieving a +0.37 IoU improvement over MAIRA-2 in anatomy-grounded report generation, more than doubling localization accuracy. Finally, CURE reduces hallucinations by 18.6% across key anatomical regions, halves contradiction rates, and more than doubles entailment with ground-truth reports, demonstrating measurable progress in improving grounding accuracy and

clinical faithfulness in medical VLMs.

Acknowledgments

This work was conducted while P. Messina was a remote research intern at the Image and Video Understanding Lab (IVUL) at KAUST, under the supervision of B. Ghanem. P. Messina was supported by the ANID Scholarship Program (Doctorado Becas Chile 2019-21191569). This work was also funded by ANID - Millennium Science Initiative Program - ICN2021_004 (iHEALTH), and by the National Center for Artificial Intelligence (CENIA) FB210017, Basal Funds for Centers of Excellence (ANID).

References

- [1] Shuai Bai, Keqin Chen, Xuejing Liu, Jialin Wang, Wenbin Ge, Sibo Song, Kai Dang, Peng Wang, Shijie Wang, Jun Tang, Humen Zhong, Yuanzhi Zhu, Mingkun Yang, Zhao-hai Li, Jianqiang Wan, Pengfei Wang, Wei Ding, Zheren Fu, Yiheng Xu, Jiabo Ye, Xi Zhang, Tianbao Xie, Zesen Cheng, Hang Zhang, Zhibo Yang, Haiyang Xu, and Junyang Lin. Qwen2.5-vl technical report. *arXiv preprint arXiv:2502.13923*, 2025. 1
- [2] Shruthi Bannur, Kenza Bouzid, Daniel C Castro, Anton Schwaighofer, Anja Thieme, Sam Bond-Taylor, Maximilian Ilse, Fernando Pérez-García, Valentina Salvatelli, Harshita Sharma, et al. Maira-2: Grounded radiology report generation. *arXiv preprint arXiv:2406.04449*, 2024. 2, 5
- [3] Shruthi Bannur, Kenza Bouzid, Daniel Coelho de Castro, Anton Schwaighofer, Sam Bond-Taylor, Maximilian Ilse, Fernando Pérez-García, Valentina Salvatelli, Harshita Sharma, Felix Meissen, Mercy Ranjit, Shaury Srivastav, Julia Gong, Fabian Falck, Ozan Oktay, Anja Thieme, Matthew P Lungren, Maria Teodora Wetscherek, Javier Alvarez-Valle, and Stephanie Hyland. Maira-2: Grounded radiology report generation. Technical Report MSR-TR-2024-18, Microsoft, 2024. 1, 6, 22
- [4] Yoshua Bengio, Jérôme Louradour, Ronan Collobert, and Jason Weston. Curriculum learning. In *Proceedings of the 26th annual international conference on machine learning*, pages 41–48, 2009. 2
- [5] Benedikt Boecking, Naoto Usuyama, Shruthi Bannur, Daniel Coelho de Castro, Anton Schwaighofer, Stephanie Hyland, Harshita Sharma, Maria Teodora Wetscherek, Tristan Naumann, Aditya Nori, Javier Alvarez Valle, Hoifung Poon, and Ozan Oktay. Ms-cxr: Making the most of text semantics to improve biomedical vision-language processing (version 1.1.0). *PhysioNet*, 2024. 3, 5
- [6] Arnaud Boutillon, Pierre-Henri Conze, Christelle Pons, Valérie Burdin, and Bhushan Borotikar. Multi-task, multi-domain deep segmentation with shared representations and contrastive regularization for sparse pediatric datasets. In *International Conference on Medical Image Computing and Computer-Assisted Intervention*, pages 239–249. Springer, 2021. 2
- [7] Alexander Buslaev, Vladimir I Iglovikov, Eugene Khvedchenya, Alex Parinov, Mikhail Druzhinin, and Alexandr A Kalinin. Albumentations: fast and flexible image augmentations. *Information*, 11(2):125, 2020. 13
- [8] Rich Caruana. Multitask learning: A knowledge-based source of inductive bias1. In *Proceedings of the Tenth International Conference on Machine Learning*, pages 41–48, 1993. 2
- [9] Chen Chen, Wenjia Bai, and Daniel Rueckert. Multi-task learning for left atrial segmentation on ge-mri. In *International workshop on statistical atlases and computational models of the heart*, pages 292–301. Springer, 2018. 2
- [10] Federico Cocchi, Nicholas Moratelli, Davide Caffagni, Sara Sarto, Lorenzo Baraldi, Marcella Cornia, and Rita Cucchiara. LLAVA-MORE: A Comparative Study of LLMs and Visual Backbones for Enhanced Visual Instruction Tuning. In *ICCVW*, 2025. 1
- [11] Daniel Coelho de Castro, Aurelia Bustos, Shruthi Bannur, Stephanie L Hyland, Kenza Bouzid, Maria Teodora Wetscherek, Maria Dolores Sánchez-Valverde, Lara Jaques-Pérez, Lourdes Pérez-Rodríguez, Kenji Takeda, et al. Padchest-gr: A bilingual chest x-ray dataset for grounded radiology report generation. *NEJM AI*, 2(7):AIdbp2401120, 2025. 3, 5, 8
- [12] Jean-Benoit Delbrouck, Pierre Chambon, Zhihong Chen, Maya Varma, Andrew Johnston, Louis Blankemeier, Dave Van Veen, Tan Bui, Steven Truong, and Curtis Langlotz. RadGraph-XL: A large-scale expert-annotated dataset for entity and relation extraction from radiology reports. In *Findings of the Association for Computational Linguistics ACL 2024*, pages 12902–12915, Bangkok, Thailand and virtual meeting, 2024. Association for Computational Linguistics. 5, 16
- [13] Guy Hacohen and Daphna Weinshall. On the power of curriculum learning in training deep networks. In *International conference on machine learning*, pages 2535–2544. PMLR, 2019. 3
- [14] Edward J Hu, Yelong Shen, Phillip Wallis, Zeyuan Allen-Zhu, Yuanzhi Li, Shean Wang, Lu Wang, Weizhu Chen, et al. Lora: Low-rank adaptation of large language models. *ICLR*, 1(2):3, 2022. 5
- [15] Daniel P Jeong, Saurabh Garg, Zachary Chase Lipton, and Michael Oberst. Medical adaptation of large language and vision-language models: Are we making progress? In *Proceedings of the 2024 Conference on Empirical Methods in Natural Language Processing*, pages 12143–12170, 2024. 2
- [16] Lu Jiang, Deyu Meng, Qian Zhao, Shiguang Shan, and Alexander Hauptmann. Self-paced curriculum learning. In *Proceedings of the AAAI Conference on Artificial Intelligence*, 2015. 2
- [17] Alistair E. W. Johnson, Tom J. Pollard, Roger G. Mark, Seth J. Berkowitz, and Steven Horng. Mimic-cxr database (version 2.1.0). *PhysioNet*, 2024. 5
- [18] Béria Chingnabé Kalpélbé, Angel Gabriel Adaambiik, and Wei Peng. Vision language models in medicine. *arXiv preprint arXiv:2503.01863*, 2025. 2
- [19] Alex Kendall, Yarin Gal, and Roberto Cipolla. Multi-task learning using uncertainty to weigh losses for scene geometry and semantics. In *Proceedings of the IEEE conference on*

computer vision and pattern recognition, pages 7482–7491, 2018. 2

[20] Sangwook Kim, Thomas G Purdie, and Chris McIntosh. Cross-task attention network: Improving multi-task learning for medical imaging applications. In *International Conference on Medical Image Computing and Computer-Assisted Intervention*, pages 119–128. Springer, 2023. 2

[21] M Kumar, Benjamin Packer, and Daphne Koller. Self-paced learning for latent variable models. *Advances in neural information processing systems*, 23, 2010. 2

[22] Chaoyi Li, Meng Li, Can Peng, and Brian C Lovell. Dynamic curriculum learning via in-domain uncertainty for medical image classification. In *International conference on medical image computing and computer-assisted intervention*, pages 747–757. Springer, 2023. 2

[23] Chunyuan Li, Cliff Wong, Sheng Zhang, Naoto Usuyama, Haotian Liu, Jianwei Yang, Tristan Naumann, Hoifung Poon, and Jianfeng Gao. Llava-med: Training a large language-and-vision assistant for biomedicine in one day. *NeurIPS*, 36:28541–28564, 2023. 1

[24] Yifan Li, Yifan Du, Kun Zhou, Jinpeng Wang, Wayne Xin Zhao, and Ji-Rong Wen. Evaluating object hallucination in large vision-language models. *arXiv preprint arXiv:2305.10355*, 2023. 1

[25] Haotian Liu, Chunyuan Li, Yuheng Li, and Yong Jae Lee. Improved baselines with visual instruction tuning. In *CVPR*, pages 26296–26306, 2024. 1

[26] Yajing Liu, Yuning Lu, Hao Liu, Yaozu An, Zhuoran Xu, Zhuokun Yao, Baofeng Zhang, Zhiwei Xiong, and Chenguang Gui. Hierarchical prompt learning for multi-task learning. In *Proceedings of the IEEE/CVF conference on computer vision and pattern recognition*, pages 10888–10898, 2023. 2

[27] Ilya Loshchilov and Frank Hutter. Decoupled weight decay regularization. *ICLR*, 2019. 5

[28] Pablo Messina, Rene Vidal, Denis Parra, Alvaro Soto, and Vladimir Araujo. Extracting and encoding: Leveraging large language models and medical knowledge to enhance radiological text representation. In *Findings of the Association for Computational Linguistics: ACL 2024*, pages 3955–3986, Bangkok, Thailand, 2024. Association for Computational Linguistics. 5, 16

[29] Pablo Messina, René Vidal, Denis Parra, Álvaro Soto, and Vladimir Araujo. Extracting and encoding: Leveraging large language models and medical knowledge to enhance radiological text representation. *arXiv preprint arXiv:2407.01948*, 2024. 3

[30] Youssef Mohamed, Noran Mohamed, Khaled Abouhashad, Feilong Tang, Sara Atito, Shoaib Jameel, Imran Razzak, and Ahmed B Zaky. Deepchest: Dynamic gradient-free task weighting for effective multi-task learning in chest x-ray classification. *arXiv preprint arXiv:2505.23595*, 2025. 2

[31] Vishwesh Nath, Wenqi Li, Dong Yang, Andriy Myronenko, Mingxin Zheng, Yao Lu, Zhijian Liu, Hongxu Yin, Yee Man Law, Yucheng Tang, et al. Vila-m3: Enhancing vision-language models with medical expert knowledge. In *Proceedings of the Computer Vision and Pattern Recognition Conference*, pages 14788–14798, 2025. 2

[32] Ha Q. Nguyen, Khanh Lam, Linh T. Le, Hieu H. Pham, Dat Q. Tran, Dung B. Nguyen, Dung D. Le, Chi M. Pham, Hang T. T. Tong, Diep H. Dinh, Cuong D. Do, Luu T. Doan, Cuong N. Nguyen, Binh T. Nguyen, Que V. Nguyen, Au D. Hoang, Hien N. Phan, Anh T. Nguyen, Phuong H. Ho, Dat T. Ngo, Nghia T. Nguyen, Nhan T. Nguyen, Minh Dao, and Van Vu. Vindr-cxr: An open dataset of chest x-rays with radiologist’s annotations, 2020. 5, 16

[33] Aaron Nicolson, Jinghui Liu, Jason Dowling, Anthony Nguyen, and Bevan Koopman. e-health CSIRO at RRG24: Entropy-augmented self-critical sequence training for radiology report generation. In *Proceedings of the 23rd Workshop on Biomedical Natural Language Processing*, pages 99–104, Bangkok, Thailand, 2024. Association for Computational Linguistics. 6, 23, 24

[34] Adam Paszke, Sam Gross, Francisco Massa, Adam Lerer, James Bradbury, Gregory Chanan, Trevor Killeen, Zeming Lin, Natalia Gimelshein, Luca Antiga, et al. Pytorch: An imperative style, high-performance deep learning library. In *Advances in Neural Information Processing Systems*, pages 8024–8035, 2019. 12

[35] Alec Radford, Jong Wook Kim, Chris Hallacy, Aditya Ramesh, Gabriel Goh, Sandhini Agarwal, Girish Sastry, Amanda Askell, Pamela Mishkin, Jack Clark, et al. Learning transferable visual models from natural language supervision. In *ICML*, pages 8748–8763. PMLR, 2021. 1

[36] Maria V Sainz de Cea, Karl Diedrich, Ran Bakalo, Lior Ness, and David Richmond. Multi-task learning for detection and classification of cancer in screening mammography. In *International conference on medical image computing and computer-assisted intervention*, pages 241–250. Springer, 2020. 2

[37] Karen Sanchez, Carlos Hinojosa, Henry Arguello, Denis Kouamé, Olivier Meyrignac, and Adrian Basarab. Cx-dagan: Domain adaptation for pneumonia diagnosis on a small chest x-ray dataset. *IEEE Transactions on Medical Imaging*, 41(11):3278–3288, 2022. 3

[38] Andrew Sellergren, Sahar Kazemzadeh, Tiam Jaroensri, Atilla Kiraly, Madeleine Traverse, Timo Kohlberger, Shawn Xu, Fayaz Jamil, Cian Hughes, Charles Lau, et al. Medgemma technical report. *arXiv preprint arXiv:2507.05201*, 2025. 1, 5

[39] Andrew Sellergren, Sahar Kazemzadeh, Tiam Jaroensri, Atilla Kiraly, Madeleine Traverse, Timo Kohlberger, Shawn Xu, Fayaz Jamil, Cian Hughes, Charles Lau, et al. Medgemma technical report. *arXiv preprint arXiv:2507.05201*, 2025. 2

[40] Ozan Sener and Vladlen Koltun. Multi-task learning as multi-objective optimization. *Advances in neural information processing systems*, 31, 2018. 2

[41] Athira Kalladayil Shibu, Sriprabha Ramanarayanan, Vinoth Kanna, Jaikishan Jayakumar, Keerthi Ram, and Mohanasankar Sivaprakasam. Medsam-guided curriculum learning for white matter tract segmentation in block face imaging of fetal brain. In *Proceedings of the IEEE/CVF International Conference on Computer Vision*, pages 1034–1041, 2025. 2

[42] Karan Singhal, Shekoofeh Azizi, Tao Tu, S Sara Mahdavi, Jason Wei, Hyung Won Chung, Nathan Scales, Ajay Tanwani, Heather Cole-Lewis, Stephen Pfahl, et al. Large language models encode clinical knowledge. *Nature*, 620(7972):172–180, 2023. 2

[43] Karan Singhal, Tao Tu, Juraj Gottweis, Rory Sayres, Ellery Wulczyn, Mohamed Amin, Le Hou, Kevin Clark, Stephen R Pfahl, Heather Cole-Lewis, et al. Toward expert-level medical question answering with large language models. *Nature Medicine*, 31(3):943–950, 2025. 2

[44] Akshay Smit, Saahil Jain, Pranav Rajpurkar, Anuj Pareek, Andrew Ng, and Matthew Lungren. Combining automatic labelers and expert annotations for accurate radiology report labeling using BERT. In *Proceedings of the 2020 Conference on Empirical Methods in Natural Language Processing (EMNLP)*, pages 1500–1519, Online, 2020. Association for Computational Linguistics. 5, 16

[45] Shengbang Tong, Zhuang Liu, Yuxiang Zhai, Yi Ma, Yann LeCun, and Saining Xie. Eyes wide shut? exploring the visual shortcomings of multimodal llms. In *CVPR*, pages 9568–9578, 2024. 1

[46] Michael Tschannen, Alexey Gritsenko, Xiao Wang, Muhammad Ferjad Naeem, Ibrahim Alabdulmohsin, Nikhil Parthasarathy, Talfan Evans, Lucas Beyer, Ye Xia, Basil Mustafa, et al. Siglip 2: Multilingual vision-language encoders with improved semantic understanding, localization, and dense features. *arXiv preprint arXiv:2502.14786*, 2025. 1

[47] Andrés Villa, Juan León Alcázar, Motasem Alfarra, Vladimir Araujo, Alvaro Soto, and Bernard Ghanem. Eagle: Enhanced visual grounding minimizes hallucinations in instructional multimodal models. *arXiv preprint arXiv:2501.02699*, 2025. 1

[48] Andrés Villa, Juan Léon, Alvaro Soto, and Bernard Ghanem. Behind the magic, merlim: Multi-modal evaluation benchmark for large image-language models. In *CVPRW*, pages 492–502, 2025. 1

[49] Xin Wang, Yudong Chen, and Wenwu Zhu. A survey on curriculum learning. *IEEE transactions on pattern analysis and machine intelligence*, 44(9):4555–4576, 2021. 2

[50] Leon Weninger, Qianyu Liu, and Dorit Merhof. Multi-task learning for brain tumor segmentation. In *International MICCAI brainlesion workshop*, pages 327–337. Springer, 2019. 2

[51] Maria Wimmer, Gert Sluiter, David Major, Dimitrios Lenis, Astrid Berg, Theresa Neubauer, and Katja Bühler. Multi-task fusion for improving mammography screening data classification. *IEEE Transactions on Medical Imaging*, 41(4):937–950, 2021. 2

[52] Thomas Wolf, Lysandre Debut, Victor Sanh, Julien Chau- mond, Clement Delangue, Anthony Moi, Pierrick Cistac, Tim Rault, Rémi Louf, Morgan Funtowicz, et al. Huggingface’s transformers: State-of-the-art natural language processing. *arXiv preprint arXiv:1910.03771*, 2019. 12

[53] Joy T. Wu, Nkechinyere N. Agu, Ismini Lourentzou, Arjun Sharma, Joseph A. Paguio, Jasper S. Yao, Edward C. Dee, William Mitchell, Satyananda Kashyap, Andrea Giovannini, Leo A. Celi, Tanveer Syeda-Mahmood, and Mehdi Moradi. Chest imangenome dataset (version 1.0.0). *PhysioNet*, 2021. 3, 5

[54] Tianhe Yu, Saurabh Kumar, Abhishek Gupta, Sergey Levine, Karol Hausman, and Chelsea Finn. Gradient surgery for multi-task learning. *Advances in neural information processing systems*, 33:5824–5836, 2020. 2

[55] Juan Manuel Zambrano Chaves, Shih-Cheng Huang, Yanbo Xu, Hanwen Xu, Naoto Usuyama, Sheng Zhang, Fei Wang, Yujia Xie, Mahmoud Khademi, Ziyi Yang, Hany Awadalla, Julia Gong, Houdong Hu, Jianwei Yang, Chunyuan Li, Jianfeng Gao, Yu Gu, Cliff Wong, Mu Wei, Tristan Naumann, Muhamao Chen, Matthew P. Lungren, Akshay Chaudhari, Serena Yeung-Levy, Curtis P. Langlotz, Sheng Wang, and Hoifung Poon. A clinically accessible small multimodal radiology model and evaluation metric for chest x-ray findings. *Nature Communications*, 16(1):3108, 2025. 1

[56] Yu Zhang and Qiang Yang. A survey on multi-task learning. *IEEE transactions on knowledge and data engineering*, 34(12):5586–5609, 2021. 2

[57] Weike Zhao, Chaoyi Wu, Xiaoman Zhang, Ya Zhang, Yanfeng Wang, and Weidi Xie. RaTEScore: A metric for radiology report generation. In *Proceedings of the 2024 Conference on Empirical Methods in Natural Language Processing*, pages 15004–15019, Miami, Florida, USA, 2024. Association for Computational Linguistics. 16

[58] Karel Zuiderveld. Contrast limited adaptive histogram equalization. In *Graphics gems IV*, pages 474–485. 1994. 5

CURE: Curriculum-guided Multi-task Training for Reliable Anatomy Grounded Report Generation

Supplementary Material

6. Implementation and Training Details

This section provides a detailed overview of the experimental setup, including hardware, hyperparameters, and the curriculum learning configuration to ensure full reproducibility.

6.1. Model and Hardware Setup

Our framework is implemented in PyTorch [34] using the Hugging Face ecosystem [52], particularly the SFT-Trainer from the TRL library for supervised fine-tuning. All experiments were conducted within a SLURM-managed High-Performance Computing (HPC) cluster equipped with NVIDIA RTX A6000 GPUs, each providing 48 GB of VRAM.

Each training run for our final model was executed on a single GPU with 60 GB of system memory RAM. The total training time for the final 9000-step CURE model was approximately 45 hours, comprising a 15-hour pre-training stage (3000 steps) followed by a 30-hour multi-task fine-tuning stage (6000 steps).

6.2. Hyperparameter Details

The training process is divided into two main phases: a 3000-step pre-training stage exclusively on the Chest Imagenet dataset, followed by a 6000-step multi-task fine-tuning phase. Key hyperparameters, which remained consistent across both stages unless otherwise noted, are detailed in Table 8. The optimizer and scheduler states were reset between the pre-training and multi-task phases, with the final checkpoint from the pre-training stage used to initialize the model weights for the subsequent phase.

6.3. Curriculum Learning Details

Our curriculum learning framework is designed to be flexible and is applied during the multi-task fine-tuning phase. The general protocol consists of two types of stages:

1. **Initial Warm-up Stage:** The training begins with a warm-up phase of N steps where all datasets and intra-dataset categories are sampled uniformly. This ensures the model receives balanced exposure to all tasks, establishing a stable performance baseline before adaptation begins.
2. **Cyclic Re-weighting Stages:** Following the warm-up, the framework enters a cyclic process. At the beginning of each subsequent stage (e.g., every M steps), the model's performance is evaluated on validation sets, and the sampling weights are recalculated and applied for

Table 8. **Hyperparameter Configuration.** Detailed hyperparameters for the pre-training and multi-task fine-tuning stages.

Hyperparameter	Value
Model & Training	
Base Model	MedGemma-4B-IT
Quantization	4-bit NF4
Precision	BF16
Optimizer	Fused AdamW
Learning Rate	2×10^{-4}
LR Scheduler	Linear
Warmup Ratio	0.03
Batch Size (per device)	5
Gradient Accum. Steps	5
Effective Batch Size	25
Max Grad Norm	0.3
LoRA Configuration	
Rank (r)	16
Alpha (α)	32
Dropout	0.05
Target Modules	All linear layers
Modules to Save	lm_head, embed_tokens

that stage. This allows the curriculum to adapt periodically to the model's evolving error profile.

While our framework supports a fully cyclic re-weighting schedule, our ablation studies (Table 7) indicated that the most effective and stable configuration for our final CURE model consisted of a single warm-up stage followed by a single re-weighting stage. Specifically, the protocol was:

- **3000 steps of warm-up** with uniform sampling.
- **3000 steps of re-weighting**, where sampling weights were calculated once after the warm-up and then fixed for the remainder of training.

The re-weighting mechanism itself operates at two levels of granularity:

Inter-Dataset Curriculum. An aggregate performance score s_i is computed for each data source D_i using a weighted average of localization and semantic metrics:

$$s_i = \alpha \cdot \text{IoU}_i + (1 - \alpha) \cdot \text{CXRFEScore}_i, \quad (3)$$

where we set $\alpha = 0.8$ to prioritize improvements in localization accuracy. The error $e_i = 1 - s_i$ is then used to update the sampling probabilities for each dataset.

Intra-Dataset Curriculum. Within each dataset, the curriculum re-weights samples at a finer, category-based level (e.g., the 8 phrase classes in MS-CXR) based on their per-class IoU. This directs the model to focus on specific concepts it finds challenging.

To provide a more granular visualization of the curriculum’s adaptive mechanism, Figures 4 and 5 illustrate the weight evolution from an experiment with a more frequent re-weighting schedule (every 500 steps). While this specific timing differs from our final CURE model, these plots clearly demonstrate the dynamic nature of the framework in action.

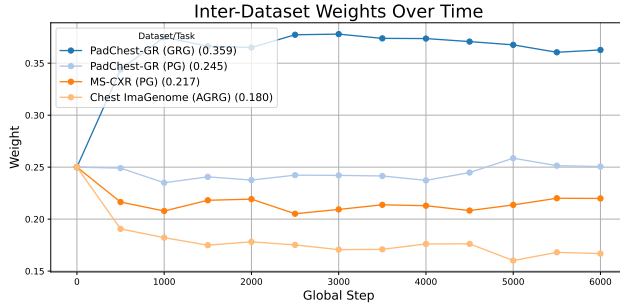


Figure 4. Visualization of Inter-Dataset Weight Dynamics. This plot illustrates the curriculum’s adaptation from an experiment with frequent updates (every 500 steps). It shows how sampling probabilities for each data source evolve over time in response to the model’s performance.

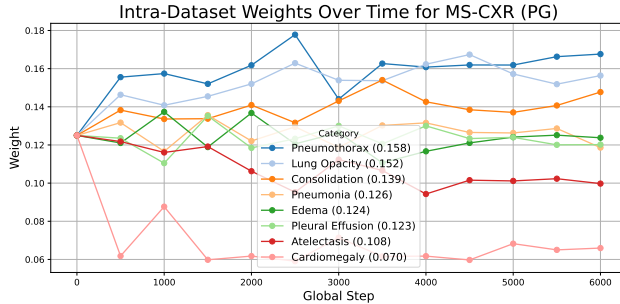


Figure 5. Visualization of Intra-Dataset Weight Dynamics for MS-CXR. This plot shows the category-level weight evolution for the 8 phrase classes in MS-CXR, taken from the same experiment with updates every 500 steps. The weights are periodically adjusted to prioritize classes with higher error rates.

7. Datasets and Task Formulation

7.1. Detailed Task I/O Formats

Table 9 provides representative examples of the instructional prompts and expected output formats for each dataset and task used during training and evaluation.

7.2. Dataset Preprocessing and Splits

We used the official train, validation, and test splits provided by each dataset. All images were processed using a custom pipeline built with the Albumentations library [7] and resized to a final resolution of 448×448 pixels. The specific image transformations varied between the training and validation/test phases to ensure data diversity during training and deterministic evaluation.

Training Pipeline. The training pipeline is stochastic, designed to improve model robustness to variations in X-ray acquisition. For each training image, the following transformations are applied:

- **CLAHE:** Applied with a 50% probability to simulate varying contrast levels, using a random clip limit uniformly sampled between 1.0 and 4.0, and a fixed tile grid size of $(8, 8)$.
- **Spatial Augmentations:** Spatial transformations included random resized cropping (30% probability) and affine transformations (translation, scaling up to $\pm 10\%$, and rotation up to $\pm 15^\circ$) applied with a 50% probability. Horizontal flipping was disabled due to the inherent left-right asymmetry of thoracic anatomy. Color-based augmentations such as jitter or Gaussian noise were explicitly disabled.
- **Regularization:** To improve stability, 30% of the training samples bypassed the spatial augmentations and instead used the deterministic validation pipeline described below.

Crucially, the entire training pipeline is bounding box-aware. When spatial transformations are applied, Albumentations simultaneously transforms the corresponding bounding box coordinates. To preserve alignment between the visual and textual modalities, the ground-truth text supervision provided to the MedGemma model is dynamically updated to reflect the augmented coordinates before training. This ensures that every augmented image remains correctly paired with its corresponding, spatially consistent text supervision.

Validation and Test Pipeline. The validation and test pipelines are deterministic. Unlike the stochastic training pipeline, these splits utilized Contrast-Limited Adaptive Histogram Equalization (CLAHE) as a fixed preprocessing normalization step rather than an augmentation. Given the high dynamic range and variable exposure settings inherent to Chest X-rays, applying deterministic CLAHE (clip limit 3.0, tile grid size $(8, 8)$) standardizes the local contrast distribution across all evaluation samples. This ensures that fine-grained clinical features—which are often obscured in low-contrast regions—are enhanced consistently for the visual encoder during inference. Finally, images were resized to 448×448 pixels.

Table 9. Summary of Datasets, Tasks, and I/O Formats. PG = Phrase Grounding; GRG = Grounded Report Generation; AGRG = Anatomy-Grounded Report Generation; RG = Report Generation. The table illustrates representative prompts and output formats for each dataset. Bounding boxes are denoted as [center_x, center_y, width, height]. For MIMIC-CXR (evaluation only), reports are generated using the GRG, AGRG, or hybrid AGRG+GRG approaches, and subsequently post-processed to remove bounding box coordinates prior to text-based evaluation.

Dataset	Task	Prompt	Example Output
MS-CXR	PG	Ground the phrase: {phrase}: {phrase}	{phrase}: [cx ₁ , cy ₁ , w ₁ , h ₁] [cx ₂ , cy ₂ , w ₂ , h ₂] ...
PadChest-GR	PG	Ground the phrase: {phrase}	{phrase}: [cx ₁ , cy ₁ , w ₁ , h ₁] [cx ₂ , cy ₂ , w ₂ , h ₂] ...
	GRG	Generate a grounded report.	Slight residual atelectasis in the right pulmonary base [0.29, 0.66, 0.18, 0.20]. Minimal blunting of the costophrenic angle [0.81, 0.74, 0.33, 0.39].
Chest ImaGenome	AGRG	Locate and describe the {location}.	Location of the abdomen: [0.48, 0.78, 0.73, 0.45]. Description: No free air below the right hemidiaphragm is seen.
		Locate the {location}.	Location of the right cardiophrenic angle: [0.33, 0.71, 0.09, 0.12].
		Describe the {location}.	Description of the left chest wall: Left chest wall pacer defibrillator is unchanged in position.
VinDr-CXR (Eval., zero-shot)	PG	Ground the phrase: {phrase}	Cardiomegaly: [0.57, 0.65, 0.55, 0.37]
	GRG	Generate a grounded report.	Consolidation [0.29, 0.54, 0.18, 0.13]. Infiltration [0.27, 0.49, 0.27, 0.24]. Pleural effusion [0.82, 0.72, 0.25, 0.14].
MIMIC-CXR (Eval.)	RG via GRG	Generate a grounded report.	{Grounded report}
	RG via AGRG	Locate and describe the {location}. ($\times N$ anatomical locations)	{Report for location 1} ... {Report for location N}
	RG via AGRG + GRG	Combine AGRG and GRG generations.	{Report for location 1} ... {Report for location N} {GRG report}

7.3. Chest ImaGenome Evaluation Benchmark

We strictly adhered to the official MIMIC-CXR data splits. As detailed in the main text, the Chest ImaGenome dataset provides scene graphs for frontal-view images in MIMIC-CXR, linking anatomical bounding boxes to textual descriptions. While we utilized the original Chest ImaGenome annotations (text snippets and bounding boxes) directly for the large-scale training and validation of the Anatomy-Grounded Report Generation (AGR) task, we devised a rigorous protocol for the test phase to ensure both computational feasibility and high-quality metric calculation.

Computational Constraints and Subsampling. Extracting all valid (image, location) pairs from the scene graphs of the official MIMIC-CXR test set yields a large pool of approximately 123,000 evaluation instances derived from 3,403 unique frontal-view images. While a comprehensive evaluation on the full set is theoretically ideal, it presents significant pragmatic challenges due to the inference latency of large multimodal models.

For example, generating anatomy-grounded reports for 1000 image-location pairs using a fine-tuned MedGemma-4B-IT takes approximately 1 hour and 20 minutes. Extrapolating this to the full test set results in roughly 164 hours (nearly a week) of continuous inference time for a single model evaluation. To facilitate faster experimentation without sacrificing statistical rigor, we curated a representative, stratified subset of 1000 samples. This subset served as a fixed artifact, ensuring that all models in our experiments were evaluated on the same diverse set of examples.

Generating High-Quality Textual Ground Truth for Evaluation. For the test subset, we sought to improve the granularity and quality of the textual ground truth. The original Chest ImaGenome dataset employs a pre-LLM NLP pipeline to associate radiology report snippets with anatomical locations. While sufficient for large-scale training, these snippets can be somewhat noisy, as they consist of raw fragments from the original radiology report and may include details not strictly related to the specified anatomical location. Moreover, they were not generated using modern language models capable of producing concise, location-tailored phrasing.

To establish a robust reference standard for evaluation metrics, we maintained the original ground-truth bounding boxes but enhanced the textual annotations. We utilized `gemini-2.5-flash-lite` to synthesize concise, location-specific “mini-reports” derived directly from the complete original radiology reports. This ensures the model is evaluated against coherent, radiologist-style descriptions that are explicitly relevant to each anatomical region of interest. The Gemini-generated mini-reports were used only

as evaluation ground truth, never for training. The prompt used for this refinement is detailed below:

```
You will be provided with a chest x-ray report and a specified anatomical location. Your task is to generate a JSON object in the following format:  
{"reasoning": "", "mini-report": ""}
```

Guidelines:

- **reasoning:** Begin your reasoning by identifying and naming anatomical regions in close proximity to the specified location. Then, briefly summarize the report as a sequence of findings/observations. Lastly, identify all findings relevant to the specified location. A finding or observation is relevant if it meets any of the following criteria: (1) it explicitly describes the specified anatomical location; (2) it explicitly describes a region anatomically very close to the specified location, where the description is highly likely to also apply to the specified location; (3) it makes a general description from which it logically and with absolute certainty follows that the description applies to the specified location as a specific instance (e.g., "both lungs are clear" implies "the right lung is clear"; "no bone abnormalities" implies "the right clavicle presents no abnormalities"); or (4) it describes devices, tubes, or other objects traversing or situated within the specified anatomical location. Present your reasoning as a single, continuous paragraph, strictly avoiding newlines and special characters.
- **mini-report:** From the relevant information identified in your reasoning, synthesize a concise and accurate mini-report, written in a style consistent with a radiologist's findings, specifically detailing the findings related to the specified anatomical location.
- If the report contains no findings or descriptions pertinent to the specified anatomical location, set the value of "mini-report" to "N/A".
- Make sure to use JSON format as shown above.

Stratified Sampling Strategy. The full test pool consists of 35,042 image-location pairs that contain descriptive findings and a larger set of image-location pairs annotated only with bounding boxes (i.e., normal or unmentioned regions). To construct the 1000-sample benchmark, we selected 700 instances with descriptive findings and 300 without.

To ensure the subset was representative of the broader test distribution, we applied a stratified sampling strategy. We generated structured annotations for the candidate mini-reports using `gemini-2.5-flash-lite` to label the presence of abnormalities and medical devices:

```
You will be provided with a chest X-ray report or sentence. Your task is to analyze the text and determine:
```

1. Whether any abnormalities or pathologies are mentioned.
2. Whether any medical devices or foreign objects are mentioned.

Output format:
Return a JSON object with the following fields:

```
{  
  "reason": "A brief explanation of your reasoning.",  
  "abnormalities": [
```

```

"mentions_abnormalities": "yes" | "no",
"mentions_devices": "yes" | "no"
}

```

Using these labels, the 700-sample partition was balanced across anatomical locations, abnormality status, and the presence of medical devices. The 300-sample partition (without specific findings) was sampled uniformly across anatomical locations to preserve anatomical diversity. This procedure yields a balanced evaluation benchmark derived strictly from the official test split.

7.4. VinDr-CXR for Zero-Shot Generalization

To assess model robustness against domain shifts and unseen data distributions, we employ the VinDr-CXR dataset [32] as a zero-shot benchmark.

Dataset Characteristics. VinDr-CXR consists of 15,000 training and 3000 testing frontal-view Chest X-rays. Each image was annotated by a consensus of three radiologists for the presence of 28 common thoracic diseases and findings. These findings are categorized into 22 localizable classes (annotated with bounding boxes) and 6 global classes (image-level labels only).

Zero-Shot Protocol. We exclude the VinDr-CXR training set entirely. None of the models evaluated in this work (including CURE and all baselines) were trained or fine-tuned on any portion of VinDr-CXR. Consequently, all results reported on this dataset reflect pure zero-shot transfer capabilities.

Task Adaptation. Since VinDr-CXR provides structured classification and detection labels rather than narrative radiology reports, we adapted the annotations to align with our text-based generation tasks:

- **Phrase Grounding (PG):** We mapped the short class labels (e.g., “ILD”, “Enlarged PA”) to full natural language phrases (e.g., “Interstitial lung disease”, “Enlarged pulmonary artery”). We generated evaluation instances for every localizable finding present in the test set, resulting in 2,108 zero-shot grounding queries.
- **Grounded Report Generation (GRG):** To create reference targets for report generation, we synthesized “pseudo-reports” from the structured annotations. For a given image, we aggregated all positive findings; localizable findings were converted into text strings containing the finding name followed by their bounding box coordinates (e.g., “Atelectasis [cx, cy, w, h]”), while global findings were appended as text-only sentences. These phrases were concatenated to form a complete, grounded target sequence, allowing us to compute both textual overlap and localization metrics.

Detailed statistics for these evaluation instances are provided in Table 1.

8. Evaluation Protocol

8.1. Metric Calculation

All metrics were computed using publicly available official implementations to ensure reproducibility.

CheXbert Metrics. We used the official CheXbert implementation [44], available at <https://pypi.org/project/f1chexbert/>, to compute clinical correctness metrics. Specifically, we report precision, recall, and F1 scores for all 14 labels under both micro and macro averaging schemes. In addition, we leveraged the BERT encoder within CheXbert to obtain dense embeddings for textual similarity analysis. Each report—both ground-truth and generated—was first segmented into individual sentences using a sentence tokenizer. The BERT model was then used to encode each sentence into an embedding vector, and we computed the cosine similarity between corresponding sentences to estimate semantic alignment. The final similarity score for a report pair was obtained by averaging these sentence-level cosine similarities, following a procedure conceptually similar to that used in CXRFEScore [28].

RadGraph F1. RadGraph-based factual consistency was evaluated using the official radgraph library [12], accessible at <https://pypi.org/project/radgraph/>. We adopted the recommended RG_ER reward as the RadGraph F1 metric, which jointly measures overlap in entity and relation predictions between generated and reference reports.

CXRFEScore. We further computed CXRFEScore [28] to assess semantic and factual consistency via structured medical knowledge representations. CXRFEScore combines two components: a fact extractor and a fact encoder. We employed the publicly released CXRFEScore models (fact extractor and fact encoder) provided by the original authors, available at <https://huggingface.co/pamessina/T5FactExtractor> and <https://huggingface.co/pamessina/CXRFEScore>, respectively. The extracted facts from both generated and ground-truth reports were encoded and compared in the resulting embedding space to produce the final factual consistency score.

RaTEScore. To assess entity-aware radiology text similarity, we utilized RaTEScore [57], available at <https://pypi.org/project/RaTEScore/>. Unlike standard lexical metrics, RaTEScore emphasizes crucial medical entities, such as diagnostic outcomes and anatomical

details, and is designed to be robust against complex medical synonyms while remaining sensitive to negation expressions. We employed the default pipeline, which utilizes a fine-tuned DeBERTa model for Medical Entity Recognition (NER) and BioLORD-2023-C for synonym disambiguation, to compute the alignment between generated and reference reports.

Bounding Box Metrics. For visual grounding evaluation, Intersection-over-Union (IoU) was computed using standard bounding box evaluation scripts. In cases where either the ground truth or the model output contained multiple bounding boxes for a given region or entity, we first merged all ground-truth boxes into a single region and likewise merged all predicted boxes, then computed IoU between the two resulting union regions. This avoids ambiguity when datasets provide multiple overlapping annotations. We report the mean IoU value across all evaluated samples (micro-average). Additionally, we calculate the average IoU per class and report the mean of these class-wise averages (macro-average).

9. Detailed Experimental Results

This section provides the complete, unabridged results from our experiments, including the full ablation study and per-task performance tables.

9.1. Extended Ablation Study

Table 10 provides detailed definitions for the model versions evaluated in our ablation study, and Table 11 presents comprehensive quantitative results. This section offers a step-by-step analysis of the training dynamics that led to the final CURE method. We examine the progression in four stages: the impact of baseline augmentations (v1–v2), the optimization of curriculum update schedules (v3–v5), the interaction between pre-training and learning rate scaling (v6–v11), and finally, a detailed isolation of sampling strategy effects (v12–v15).

Baseline and Data Augmentation (v1–v2). Our baseline model (**v1**) employs uniform sampling without augmentation. As observed in Table 11, introducing bounding-box-aware augmentation (**v2**) results in consistent, though modest, improvements in Phrase Grounding (PG) metrics across datasets (e.g., MS-CXR IoU improves from 0.389 to 0.406). This suggests that spatial transformations help the model generalize better to anatomical coordinates that may differ slightly from the training prototypes, without requiring changes to the model architecture.

Curriculum Learning Frequency (v3–v5). Configurations v3 through v5 explore the frequency of curriculum re-

weighting updates. We observe that a longer accumulation window of 3000 steps (**v5**) yields higher final performance compared to more frequent updates (1500 or 2000 steps). This indicates that the model benefits from longer exposure to a fixed data distribution, allowing performance on current tasks to plateau before the curriculum logic re-adjusts the sampling ratios.

Impact of Learning Rate on Pre-training (v6–v11). A pivotal finding is the interaction between pre-training and learning rate. In variants v6–v8 (low LR, 2e-5), Chest Imagenome (CIG) pre-training yielded only marginal gains over the baseline. However, increasing the learning rate to 2e-4 (v9–v11) unlocked substantial improvements. Comparing **v8** (Low LR) to **v11** (High LR, CURE), we observe a sharp increase in AGRG IoU (from 0.469 to **0.596**) and Phrase Grounding MS-CXR IoU (from 0.497 to 0.554). This implies that a higher learning rate is necessary to effectively adapt the visual encoder to fine-grained anatomical text after the initial pre-training phase. Among these high-LR variants, the 3000-step pre-training schedule (**v11**) provided the most consistent performance across tasks, serving as our final CURE configuration.

Sampling Strategy Analysis (v12–v15). Finally, we investigate the impact of data mixing strategies. As detailed in Section 3.1, our framework defines “data sources” as specific dataset-task pairs (e.g., PadChest-GR (task: GRG) vs. MS-CXR (task: PG)). To facilitate the analysis, we define the three sampling approaches used in variants v12–v15 as follows:

- *Natural Sampling*: At the **Inter-level**, data sources are sampled strictly proportional to their size (heavily biasing training toward Chest Imagenome). At the **Intra-level**, samples are drawn randomly without intervention, preserving the inherent clinical class imbalance.
- *Uniform Sampling*: At the **Inter-level**, all data sources are sampled with equal probability ($1/K$). At the **Intra-level**, samples are drawn such that each category (e.g., finding or anatomical region) has an equal probability of selection ($1/C$).
- *Curriculum Sampling*: Sampling probabilities are dynamically re-weighted based on error rates. At the **Inter-level**, this balances distinct data sources based on aggregate validation performance. At the **Intra-level**, this re-weights specific intra-dataset categories based on per-class error.

We analyze the impact of these strategies on both in-domain tasks and the zero-shot out-of-distribution (OOD) benchmark, VinDr-CXR.

- **The Risks of Natural Sampling (v15):** Variant **v15** employs a fully Natural strategy. While this achieves the

Table 10. **Experimental Configuration Summary.** Detailed definitions of the model configurations (v1–v15) evaluated in the ablation study (see Table 11). The table outlines the progression from the baseline model to the proposed CURE method, detailing variations in data augmentation (Aug), curriculum learning (CL) schedules, Chest Imagenome (CIG) pre-training duration, learning rates, and sampling strategies (Inter/Intra-dataset).

Model Configuration	Description
<i>— Baseline & Augmentation —</i>	
v1: Base (w/o Aug, w/o CL, w/o CIG, lr=2e-5)	Baseline: Basic multi-task fine-tuning using uniform sampling across all datasets (inter-dataset) and within datasets (intra-dataset). No data augmentation or pre-training is applied. Fine-tuned with a base learning rate of 2e-5 for 6k steps.
v2: + Aug	Identical to v1, but enables bounding-box-aware augmentations (stochastic CLAHE, RandomResizedCrop, and affine transforms). Ground-truth text coordinates are dynamically updated to match spatial changes. Horizontal flipping and color distortions are disabled.
<i>— Curriculum Learning (CL) Frequency —</i>	
v3: + Aug + CL(1.5k)	Extends v2 by introducing curriculum learning (CL). The sampling distribution is re-weighted based on model performance every 1500 steps .
v4: + Aug + CL(2k)	Same as v3, but the curriculum re-weighting interval is increased to every 2000 steps .
v5: + Aug + CL(3k)	Same as v3, but the curriculum re-weighting interval is set to every 3000 steps . This serves as the foundational CL schedule for subsequent experiments.
<i>— CIG Pre-training Integration (Low LR: 2e-5) —</i>	
v6: + Aug + CIG(1k) + CL(3k)	Introduces a pre-training phase on the Chest Imagenome (CIG) dataset for 1000 steps (lr=2e-5) before initializing the multi-task fine-tuning configuration of v5.
v7: + Aug + CIG(2k) + CL(3k)	Extends the CIG pre-training phase to 2000 steps (lr=2e-5) before fine-tuning.
v8: + Aug + CIG(3k) + CL(3k)	Extends the CIG pre-training phase to 3000 steps (lr=2e-5) before fine-tuning.
<i>— Learning Rate Scaling (High LR: 2e-4) —</i>	
v9: + Aug + CIG(1k) + CL(3k) + lr=2e-4	Replicates the structure of v6 (1k pre-train), but significantly increases the learning rate to 2e-4 for both pre-training and fine-tuning stages.
v10: + Aug + CIG(2k) + CL(3k) + lr=2e-4	Replicates the structure of v7 (2k pre-train) with the higher learning rate of 2e-4 .
v11 (CURE): + Aug + CIG(3k) + CL(3k) + lr=2e-4	Proposed Method (CURE): Replicates v8 (3k pre-train) with the higher learning rate (2e-4). Combines prolonged pre-training, high learning rate, and 3k-step curriculum updates.
<i>— Sampling Strategy Ablations (Based on v11) —</i>	
v12: + Aug + CIG(3k) + Uni(Inter)/Nat(Inter) + lr=2e-4	Modification of v11 that removes Curriculum Learning entirely. Uses Uniform sampling between datasets (Inter) and Natural distribution sampling within datasets (Intra).
v13: + Aug + CIG(3k) + CL(Inter,3k)/Nat(Inter) + lr=2e-4	Modification of v11 that applies Curriculum Learning (3k re-weighting) only to the inter-dataset sampling ratios, while maintaining a Natural distribution for intra-dataset sampling.
v14: + Aug + CIG(3k) + Uni(Inter)/CL(Inter,3k) + lr=2e-4	Modification of v11 that applies Uniform sampling between datasets (Inter), while applying Curriculum Learning (3k re-weighting) exclusively to intra-dataset sampling.
v15: + Aug + CIG(3k) + Nat(Inter)/Nat(Inter) + lr=2e-4	Modification of v11 using a fully Natural sampling strategy (proportional to dataset size) for both inter-dataset and intra-dataset distributions.

absolute highest performance on the dominant Chest Imagenome dataset (AGR IoU **0.626**), it underperforms significantly on all other tasks. Most notably, it suffers a complete collapse on Grounded Report Generation (GRG), dropping to **0.000** IoU for both PadChest and VinDr-CXR. This confirms that without explicit rebalancing, the model overfits the largest data source and fails to acquire generalizable capabilities for auxiliary tasks.

- **Uniform vs. Curriculum (v12 vs. v13):** Removing CL entirely and employing Uniform inter-dataset sampling (v12) effectively prevents the collapse seen in v15, yielding a very strong baseline that competes closely with the curriculum variants. However, applying Curriculum Learning to the inter-dataset mix (v13) offers marginal but consistent gains over the Uniform baseline across several benchmarks. For instance, v13 achieves the highest grounding performance on PadChest (GRG IoU **0.271** vs. 0.263) and MS-CXR (IoU **0.569** vs. 0.560). This suggests that while Uniform sampling provides a robust foundation, dynamic re-weighting can squeeze out minor performance improvements by prioritizing harder tasks.

- **Inter- vs. Intra-Dataset Dynamics (v13 vs. v14):** We further isolate the CL logic. Variant v13 applies CL only to the *Inter-dataset* mix, while v14 applies CL only to the *Intra-dataset* mix. Variant v13 outperforms v14 on Grounded Report Generation tasks (e.g., GRG-PC IoU **0.271** vs. 0.246). Empirically, the curriculum logic at the inter-dataset level, present in v13, tends to assign higher sampling probabilities to the GRG task, as previously seen in Figure 4, compared to uniform or intra-only strategies, likely due to the higher difficulty of generating full grounded reports. While the differences are not dramatic, the results indicate that macro-level balancing between distinct data sources (Inter-CL) is a more effective driver of robustness than fine-grained category re-weighting (Intra-CL).

Ultimately, while Uniform sampling (v12) proves to be a highly effective strategy for multi-task stability, the Curriculum-based methods (v11/v13) demonstrate the capacity to further refine performance on challenging tasks like Grounded Report Generation without compromising the baseline capabilities.

Table 11. **Extended Ablation Study.** Performance of all ablation variants across three tasks: **AGR**G (Anatomy-Grounded Report Generation on Chest ImaGenome), **GR**G (Grounded Report Generation on PadChest-GR and VinDr-CXR), and **PG** (Phrase Grounding on MS-CXR, PadChest-GR, and VinDr-CXR). Each block reports mean Intersection-over-Union (**IoU**, micro average), CheXbert F1 (micro average, **F1**), and CXRFEScore (**CXS**) metrics. Rows v1–v5 analyze the effects of data augmentation and curriculum learning (CL); v6–v8 add CIG pre-training with a low learning rate (2e-5); v9–v11 repeat those with a higher learning rate (2e-4); and v12–v15 further explore inter- and intra-dataset sampling strategies. Best results in each column are shown in **bold**, and second-best are underlined.

Dataset abbreviations: CIG = Chest ImaGenome, PC = PadChest-GR, VD = VinDr-CXR, MS = MS-CXR.

Model Configuration	AGR (CIG)			GR (PC)			GR (VD)			PG (IoU ↑)		
	IoU ↑	F1 ↑	CXS ↑	IoU ↑	F1 ↑	CXS ↑	IoU ↑	F1 ↑	CXS ↑	MS	PC	VD
MAIRA-2 (External Baseline)	0.226	0.272	0.360	0.256	0.592	0.616	0.216	0.546	0.592	0.496	0.280	0.162
v1: Base (w/o Aug, w/o CL, w/o CIG, lr=2e-5)	0.393	0.503	0.565	0.171	0.558	0.589	0.207	0.586	0.630	0.389	0.356	0.192
v2: + Aug	0.378	0.485	0.552	0.185	0.563	<u>0.602</u>	0.214	<u>0.613</u>	0.646	0.406	0.365	0.205
v3: + Aug + CL(1.5k)	0.402	0.478	0.556	0.179	0.564	0.592	0.224	0.605	0.630	0.410	0.383	0.211
v4: + Aug + CL(2k)	0.394	0.473	0.542	0.193	0.569	0.596	0.222	0.610	<u>0.651</u>	0.395	0.383	0.197
v5: + Aug + CL(3k)	0.419	0.482	0.552	0.180	<u>0.579</u>	0.596	0.217	0.626	0.671	0.432	0.393	0.205
v6: + Aug + CIG(1k) + CL(3k)	0.452	0.488	0.544	0.195	0.554	0.591	0.232	0.582	0.628	0.459	0.395	0.220
v7: + Aug + CIG(2k) + CL(3k)	0.444	0.459	0.525	0.203	0.536	0.587	0.227	0.553	0.590	0.468	0.404	0.223
v8: + Aug + CIG(3k) + CL(3k)	0.469	0.492	0.546	0.206	0.553	0.582	0.233	0.568	0.601	0.497	0.422	0.225
v9: + Aug + CIG(1k) + CL(3k) + lr=2e-4	0.591	0.487	0.549	0.253	0.523	0.563	0.258	0.491	0.529	0.566	0.454	<u>0.248</u>
v10: + Aug + CIG(2k) + CL(3k) + lr=2e-4	0.594	0.506	0.561	0.258	0.523	0.570	0.262	0.449	0.477	0.575	0.457	<u>0.249</u>
v11 (CURE): + Aug + CIG(3k) + CL(3k) + lr=2e-4	0.596	0.474	0.548	<u>0.265</u>	0.507	0.574	0.262	0.505	0.540	0.554	0.453	0.244
v12: + Aug + CIG(3k) + Uni(Inter)/Nat(Inter) + lr=2e-4	0.586	<u>0.507</u>	0.564	0.263	0.530	0.576	<u>0.264</u>	0.489	0.514	0.560	<u>0.457</u>	0.245
v13: + Aug + CIG(3k) + CL(Inter,3k)/Nat(Inter) + lr=2e-4	0.596	0.494	0.553	0.271	0.504	0.550	<u>0.266</u>	0.434	0.469	0.569	0.464	0.244
v14: + Aug + CIG(3k) + Uni(Inter)/CL(Inter,3k) + lr=2e-4	0.594	0.505	<u>0.568</u>	0.246	0.544	0.570	0.262	0.496	0.536	<u>0.557</u>	0.456	0.245
v15: + Aug + CIG(3k) + Nat(Inter)/Nat(Inter) + lr=2e-4	0.626	0.519	0.576	0.000	0.498	0.483	0.000	0.604	0.534	0.358	0.221	0.163

9.2. Full Results Tables

The following tables contain the complete, unabridged results for each evaluation task and dataset, from which the summary tables in the main paper were derived.

9.2.1. Anatomy-Grounded Report Generation (AGR)

Table 12 presents a comprehensive breakdown of performance on the Anatomy-Grounded Report Generation (AGR) task, isolating the effects of pre-training strategies and multi-task fine-tuning configurations.

Trade-offs Between Grounding and Clinical Label Accuracy. Comparing the baseline (v1) with the optimized variants (v11–v15) reveals a trade-off between spatial precision and macro-averaged label performance. The baseline model achieves the highest F1-Macro (0.323), whereas the high-performing variants achieve significantly higher IoU (> 0.58) but lower F1-Macro scores (0.25–0.31). This behavior can be attributed to our current curriculum design. For the AGR task, the intra-dataset re-weighting strategy is explicitly designed to balance *anatomical locations* to ensure robust localization, but it does not currently account for the distribution of *abnormal findings*. Consequently, while we observe consistent improvements in spatial metrics (IoU) and stable performance on domi-

nant classes (F1-Micro), the model does not currently benefit from re-balancing rare pathological conditions. This highlights a clear avenue for future work: designing a more sophisticated re-balancing strategy that simultaneously targets anatomical diversity and the distribution of rare clinical findings to improve report generation performance on long-tailed conditions.

Pre-training Efficiency. The “Chest ImaGenome (CIG) Pre-training Only” block highlights the impact of learning rate scaling. With a conservative learning rate (2e-5), extending pre-training from 1,000 to 3,000 steps yields only marginal IoU gains ($0.388 \rightarrow 0.411$). Conversely, increasing the learning rate to 2e-4 results in a substantial improvement, with the 3,000-step high-LR variant achieving an IoU of 0.582 even before multi-task fine-tuning. This confirms that aligning visual features with fine-grained anatomy-grounded reports benefits from more aggressive optimization during the initial training stages.

Performance of Sampling Strategies. Among the final sampling variants, we observe that v15 (Natural Sampling) achieves the highest scores across all metrics in this specific task (IoU **0.626**, CXS **0.576**). This result is expected given the data distribution: v15 undergoes 3,000 steps of

Table 12. **Detailed Results for Anatomy-Grounded Report Generation (AGR).** Performance of baseline models, pre-training-only checkpoints, and the full set of multi-task fine-tuning ablation variants (v1–v15) on the Chest Imagenome test subset. We report mean Intersection-over-Union (**IoU**, \uparrow), CheXbert F1 (Micro/Macro averages, \uparrow), CheXbert cosine similarity (**Cos.**, \uparrow), and CXRFEScore (**CXS**, \uparrow). **Bold** indicates the best result per column; underlined indicates the second best.

Model Variant	IoU \uparrow	F1-Mi \uparrow	F1-Ma \uparrow	Cos. \uparrow	CXS \uparrow
<i>— Baselines —</i>					
MAIRA-2	0.226	0.272	0.100	0.557	0.360
MedGemma-4B-IT	–	0.344	0.294	0.631	0.477
<i>— Chest Imagenome (CIG) Pre-training Only —</i>					
CIG Pre-train (1k steps, lr=2e-5)	0.388	0.447	0.221	0.633	0.518
CIG Pre-train (2k steps, lr=2e-5)	0.392	0.481	0.254	0.634	0.533
CIG Pre-train (3k steps, lr=2e-5)	0.411	0.488	0.267	0.648	0.549
CIG Pre-train (1k steps, lr=2e-4)	0.500	0.501	0.304	0.646	0.547
CIG Pre-train (2k steps, lr=2e-4)	0.578	0.505	<u>0.320</u>	0.666	0.561
CIG Pre-train (3k steps, lr=2e-4)	0.582	0.502	<u>0.297</u>	0.664	0.560
<i>— Multi-task Fine-tuning Variants (v1–v15) —</i>					
v1 : Base (w/o Aug, w/o CL, w/o CIG, lr=2e-5)	0.393	0.503	0.323	0.658	0.565
v2 : + Aug	0.378	0.485	0.318	0.646	0.552
v3 : + Aug + CL(1.5k)	0.402	0.478	0.281	0.648	0.556
v4 : + Aug + CL(2k)	0.394	0.473	0.284	0.636	0.542
v5 : + Aug + CL(3k)	0.419	0.482	0.287	0.649	0.552
v6 : + Aug + CIG(1k) + CL(3k)	0.452	0.488	0.278	0.636	0.544
v7 : + Aug + CIG(2k) + CL(3k)	0.444	0.459	0.245	0.633	0.525
v8 : + Aug + CIG(3k) + CL(3k)	0.469	0.492	0.293	0.648	0.546
v9 : + Aug + CIG(1k) + CL(3k) + lr=2e-4	0.591	0.487	0.306	0.655	0.549
v10 : + Aug + CIG(2k) + CL(3k) + lr=2e-4	0.594	0.506	0.266	0.654	0.561
v11 (CURE) : + Aug + CIG(3k) + CL(3k) + lr=2e-4	<u>0.596</u>	0.474	0.273	0.649	0.548
v12 : + Aug + CIG(3k) + Uni(Inter)/Nat(Inter) + lr=2e-4	<u>0.586</u>	<u>0.507</u>	0.267	0.665	0.564
v13 : + Aug + CIG(3k) + CL(Inter,3k)/Nat(Inter) + lr=2e-4	<u>0.596</u>	0.494	0.254	0.662	0.553
v14 : + Aug + CIG(3k) + Uni(Inter)/CL(Inter,3k) + lr=2e-4	0.594	0.505	0.297	<u>0.669</u>	<u>0.568</u>
v15 : + Aug + CIG(3k) + Nat(Inter)/Nat(Inter) + lr=2e-4	0.626	0.519	0.308	0.674	0.576

pre-training and 6,000 steps of fine-tuning where samples are drawn proportional to dataset size. Since Chest Imagenome dominates the training mixture, **v15** is effectively trained on AGRG for the vast majority of these \sim 9,000 steps. However, as detailed in the ablation study (Section 9.1), this specialization leads to severe degradation on complementary tasks (GRG and PG) on other datasets. The strategies that actively intervene on the data distribution—Uniform (**v12**) and the Curriculum variants (**v11**, **v13**, **v14**)—maintain competitive in-domain performance (IoU \sim 0.59, CXS \sim 0.55–0.56) while preventing the task collapse observed in **v15**. Notably, all proposed variants (v9–v15) significantly outperform the external MAIRA-2 baseline in both spatial grounding (IoU \sim 0.59–0.62 vs. 0.226) and semantic alignment (Cos. Sim. $>$ 0.65 and CXS $>$ 0.55 vs. 0.557 and 0.360, respectively).

9.2.2. Phrase Grounding (PG)

Table 13 details the Phrase Grounding performance across three diverse benchmarks: MS-CXR (in-domain), PadChest-GR (in-domain), and VinDr-CXR (zero-shot, unseen distribution).

Generalization via Augmentation. The transition from the baseline (**v1**) to the augmented variant (**v2**) highlights the utility of spatial invariance training. We observe consistent improvements across all benchmarks, with MS-CXR IoU Micro increasing from 0.389 to 0.405 and the zero-shot VinDr-CXR metric improving from 0.192 to 0.205. This suggests that bounding-box-aware augmentations assist the model in learning generalized anatomical features, reducing overfitting to the specific rigid acquisition protocols of the training data.

Progressive Improvements: Curriculum, Pre-training, and Learning Rate. The results demonstrate a cumulative benefit from each component of the CURE pipeline. First, introducing curriculum learning alone (variants **v3**–**v5**) yields a moderate gain over the augmented baseline (e.g., v5 reaches 0.432 IoU on MS-CXR vs. 0.405 for v2). Second, adding Chest Imagenome pre-training with a conservative learning rate (variants **v6**–**v8**) pushes performance further, with **v8** reaching 0.497 IoU. Finally, the most dramatic jump occurs when increasing the learning rate to 2e-4

Table 13. **Detailed Results for Phrase Grounding (PG).** We report Micro-Average IoU (**IoU Mi.** \uparrow) and Macro-Average IoU (**IoU Ma.** \uparrow) on three test sets: MS-CXR, PadChest-GR, and zero-shot VinDr-CXR. The ablation variants (v1–v15) demonstrate that high-learning-rate training (v9–v11) and advanced sampling strategies (v10, v13) yield substantial gains over the baseline and MAIRA-2. **Bold** indicates best; underlined indicates second best.

Model Variant	MS-CXR		PadChest-GR		VinDr-CXR (Zero-Shot)	
	IoU Mi. \uparrow	IoU Ma. \uparrow	IoU Mi. \uparrow	IoU Ma. \uparrow	IoU Mi. \uparrow	IoU Ma. \uparrow
MAIRA-2	0.496	0.452	0.280	0.287	0.162	0.115
v1: Base (w/o Aug, w/o CL, w/o CIG, lr=2e-5)	0.389	0.344	0.356	0.345	0.192	0.144
v2: + Aug	0.405	0.354	0.365	0.359	0.205	0.149
v3: + Aug + CL(1.5k)	0.410	0.369	0.383	0.382	0.211	0.154
v4: + Aug + CL(2k)	0.395	0.348	0.383	0.381	0.197	0.145
v5: + Aug + CL(3k)	0.432	0.376	0.393	0.397	0.205	0.155
v6: + Aug + CIG(1k) + CL(3k)	0.459	0.405	0.395	0.391	0.220	0.167
v7: + Aug + CIG(2k) + CL(3k)	0.468	0.428	0.404	0.399	0.223	0.161
v8: + Aug + CIG(3k) + CL(3k)	0.497	0.446	0.422	0.419	0.225	0.173
v9: + Aug + CIG(1k) + CL(3k) + lr=2e-4	0.566	<u>0.514</u>	0.454	0.443	0.248	0.204
v10: + Aug + CIG(2k) + CL(3k) + lr=2e-4	0.575	0.525	<u>0.457</u>	0.446	0.249	0.206
v11 (CURE): + Aug + CIG(3k) + CL(3k) + lr=2e-4	0.554	0.495	0.453	0.438	0.244	<u>0.205</u>
v12: + Aug + CIG(3k) + Uni(Inter)/Nat(Inter) + lr=2e-4	0.560	0.507	<u>0.457</u>	0.449	<u>0.245</u>	0.198
v13: + Aug + CIG(3k) + CL(Inter,3k)/Nat(Inter) + lr=2e-4	<u>0.569</u>	<u>0.514</u>	0.464	0.455	0.244	0.199
v14: + Aug + CIG(3k) + Uni(Inter)/CL(Inter,3k) + lr=2e-4	0.557	0.495	0.456	<u>0.451</u>	<u>0.245</u>	0.203
v15: + Aug + CIG(3k) + Nat(Inter)/Nat(Inter) + lr=2e-4	0.358	0.277	0.221	0.206	0.163	0.099

for *both* the pre-training and multi-task fine-tuning phases (variants **v9–v11**). Comparing **v8** (Low LR) to **v11** (High LR), we observe an improvement of over 5 points on MS-CXR ($0.497 \rightarrow 0.554$). This confirms that a higher learning rate is essential throughout the entire pipeline to fully align visual features with text and escape local minima.

Sampling Strategy Dynamics. Analyzing the sampling strategies (v10–v15) reveals distinct performance profiles across datasets:

- **Natural Sampling Failure:** Variant **v15** suffers a severe regression, dropping to 0.358 IoU on MS-CXR (worse than the un-augmented baseline v1). This confirms that without intervention, the dominance of AGRG data overwhelms the signal from smaller grounding datasets.
- **Peak Performance (v10 vs. v13):** While the proposed CURE model (**v11**) is highly competitive, the absolute peak performance for grounding is split between **v10** and **v13**. Variant **v10** (2k pre-training) achieves the highest scores on MS-CXR (**0.575**) and the zero-shot VinDr-CXR (**0.249**), suggesting that a slightly shorter pre-training phase may occasionally favor pure localization tasks. Conversely, **v13** (Inter-CL) achieves the best performance on PadChest-GR (**0.464**), indicating that dynamic inter-dataset balancing effectively captures the nuances of that specific distribution.
- **Overall Robustness:** Despite these minor variations, all high-LR curriculum variants (v10, v11, v13, v14) significantly outperform the external MAIRA-2 baseline (e.g., ~ 0.24 vs. 0.16 on VinDr-CXR), validating the general

effectiveness of the proposed framework.

9.2.3. Grounded Report Generation (GRG)

Table 14 presents the ablation results for the Grounded Report Generation (GRG) task on PadChest-GR and the zero-shot VinDr-CXR benchmark. This task is the most challenging in our suite, requiring the model to simultaneously generate a full radiology report and localize every mentioned finding.

Localization vs. Clinical Metrics. A clear divergence emerges when comparing the low-learning-rate variants (**v1–v8**) with the high-learning-rate variants (**v9–v14**). The low-LR models often achieve higher scores on clinical text metrics; for instance, **v5** achieves a zero-shot F1-Micro of **0.626** on VinDr-CXR but has limited localization accuracy (IoU 0.217). Conversely, the high-LR variants significantly boost visual grounding (e.g., **v13** reaches IoU **0.266**) but often see a regression in text metrics (F1-Micro drops to 0.434). This pattern suggests that while aggressive updates are necessary to learn the structural constraints of the GRG task (i.e., outputting bounding box coordinates), our current training protocol heavily favors the grounding objective. Future work is likely needed to design more sophisticated re-balancing strategies—such as balancing positive versus negative findings or specific finding classes—to simultaneously enhance clinical reporting metrics without sacrificing localization performance.

Table 14. **Detailed Results for Grounded Report Generation (GRG).** Performance on PadChest-GR and the zero-shot VinDr-CXR benchmark. We report mean IoU (\uparrow), CheXbert F1 (micro/macro, \uparrow), CheXbert cosine similarity (**Cos.**, \uparrow), and CXRFEScore (**CXS**, \uparrow). High-learning-rate variants (v9–v13) consistently achieve superior localization (IoU) compared to baselines. **Bold** indicates best; underlined indicates second best.

Model Variant	PadChest-GR					VinDr-CXR (Zero-Shot)				
	IoU \uparrow	F1-Mi \uparrow	F1-Ma \uparrow	Cos. \uparrow	CXS \uparrow	IoU \uparrow	F1-Mi \uparrow	F1-Ma \uparrow	Cos. \uparrow	CXS \uparrow
<i>— Baselines —</i>										
MAIRA-2	0.256	0.592	0.325	0.844	0.616	0.216	0.546	0.237	0.824	0.592
MedGemma-4B-IT	–	0.144	0.198	0.733	0.517	–	0.209	0.196	0.779	0.596
<i>— Multi-task Fine-tuning Variants (v1–v15) —</i>										
v1: Base (w/o Aug, w/o CL, w/o CIG, lr=2e-5)	0.171	0.558	0.247	0.829	0.589	0.207	0.586	0.230	0.835	0.630
v2: + Aug	0.185	0.563	0.232	0.838	<u>0.602</u>	0.214	<u>0.613</u>	<u>0.258</u>	0.832	0.646
v3: + Aug + CL(1.5k)	0.179	0.564	0.239	0.835	0.592	0.224	0.605	0.234	0.816	0.630
v4: + Aug + CL(2k)	0.193	0.569	0.247	0.838	0.596	0.222	0.610	0.230	0.842	0.651
v5: + Aug + CL(3k)	0.180	<u>0.579</u>	0.257	<u>0.843</u>	0.596	0.217	0.626	0.235	<u>0.843</u>	0.671
v6: + Aug + CIG(1k) + CL(3k)	0.195	0.554	0.279	0.837	0.591	0.232	0.582	0.260	0.838	0.628
v7: + Aug + CIG(2k) + CL(3k)	0.203	0.536	0.277	0.829	0.587	0.227	0.553	0.234	0.828	0.590
v8: + Aug + CIG(3k) + CL(3k)	0.206	0.553	0.293	0.835	0.582	0.233	0.568	0.230	0.841	0.601
v9: + Aug + CIG(1k) + CL(3k) + lr=2e-4	0.253	0.523	0.314	0.820	0.563	0.258	0.491	0.219	0.814	0.529
v10: + Aug + CIG(2k) + CL(3k) + lr=2e-4	0.258	0.523	0.265	0.820	0.570	0.262	0.449	0.218	0.799	0.477
v11 (CURE): + Aug + CIG(3k) + CL(3k) + lr=2e-4	<u>0.265</u>	0.507	0.271	0.819	0.574	0.262	0.505	0.229	0.832	0.540
v12: + Aug + CIG(3k) + Uni(Inter)/Nat(Inter) + lr=2e-4	0.263	0.530	0.277	0.824	0.576	<u>0.264</u>	0.489	0.226	0.819	0.514
v13: + Aug + CIG(3k) + CL(Inter,3k)/Nat(Inter) + lr=2e-4	0.271	0.504	0.279	0.813	0.550	0.266	0.434	0.214	0.794	0.469
v14: + Aug + CIG(3k) + Uni(Inter)/CL(Inter,3k) + lr=2e-4	0.246	0.544	<u>0.318</u>	0.824	0.570	0.262	0.496	0.228	0.815	0.536
v15: + Aug + CIG(3k) + Nat(Inter)/Nat(Inter) + lr=2e-4	0.000	0.498	0.191	0.788	0.483	0.000	0.604	0.193	0.858	0.534

Benchmarking Against MAIRA-2. The PadChest-GR results are particularly significant. This task theoretically favors the MAIRA-2 baseline, which benefits from training on both PadChest-GR and the large, proprietary USMix dataset [3] (containing $\sim 70k$ grounded reports). Despite this data disadvantage, our high-LR variants (**v10**, **v11**, **v12**, **v13**) consistently surpass MAIRA-2 in localization performance (e.g., v13 IoU **0.271** vs. 0.256). On the zero-shot VinDr-CXR benchmark, this trend holds, with most high-LR variants significantly outperforming MAIRA-2 (0.216). However, **v15** (Natural Sampling) illustrates a critical failure mode: it achieves an IoU of **0.000** on both datasets yet records the highest Cosine Similarity on VinDr-CXR (**0.858**). This suggests that the model, being overwhelmed by the dominant AGRG data (Chest Imagenet), reverts to the behavior of an AGRG model: it generates clinically plausible descriptions (transferring knowledge from training) but fails to adhere to the specific formatting requirements of the GRG task (generating coordinates for these specific datasets). The task collapse here is not necessarily a failure of visual understanding, but a failure to learn the minority task’s output format due to extreme data imbalance.

Impact of Sampling Strategies. We focus on the comparison between **v12** (Uniform Inter-sampling) and **v13** (Curriculum Inter-sampling). As noted in Section 3.1, PadChest-GR does not utilize intra-dataset curriculum re-weighting; therefore, differences in performance stem primarily from how the model balances the distinct data

sources. Variant **v13** achieves the highest IoU on both datasets, surpassing the Uniform baseline (**v12**). This indicates that dynamically up-weighting the GRG data sources (based on error rates) helps the model prioritize the visual grounding objective more effectively than static uniform sampling. While the margins are modest, **v13** consistently provides the most robust grounding performance across the evaluated benchmarks.

9.2.4. Standard Report Generation (MIMIC-CXR)

Table 15 provides a detailed breakdown of report generation performance on the MIMIC-CXR test set. We analyze how different inference protocols ranging from single-prompt generation to multi-location concatenation affect the trade-off between precision, recall, and semantic alignment.

Impact of Anatomical Granularity (N). A unique feature of the CURE framework is the ability to modulate the “resolution” of the generated report by varying the number of queried anatomical locations (N). The compositions of these sets are detailed in Table 16.

- **AGR-9 (High Precision):** By querying only 9 core locations, the model achieves high precision (P-Mi: **0.639**), comparable to the grounded reports of MAIRA-2 (P-Mi: **0.639**). This configuration also yields the highest RadGraph F1 score among the CURE variants, making it comparatively more suitable for scenarios where minimizing false positives is a priority.
- **AGR-29 (Balanced Supervision):** This set comprises the 29 anatomical locations for which Chest Imagenet provides both bounding box and text supervision. Us-

Table 15. **Results for Report Generation (RG) on the MIMIC-CXR test set.** We evaluate state-of-the-art baselines, a model fine-tuned solely for report generation (**MedGemma-FT (RG)**), and the proposed **CURE** model. Notably, since **CURE** is multi-task, we explore different inference protocols: **GRG** (generating a single grounded report), **AGR-G-N** (concatenating location-specific descriptions for N anatomical regions), and their combinations. We report CheXbert F1, Precision (P), and Recall (R) (Micro/Macro averaged), CheXbert Cosine Similarity (**Cos.**), CXRFEScore (**CXS**), RaTEScore (**RaTES**), and RadGraph F1 (**RadF1**). **Bold** and underlined values indicate the best and second-best scores.

Model / Inference Protocol	F1-Ma \uparrow	F1-Mi \uparrow	P-Ma \uparrow	P-Mi \uparrow	R-Ma \uparrow	R-Mi \uparrow	Cos. \uparrow	CXS \uparrow	RaTES \uparrow	RadF1 \uparrow
<i>— Baselines —</i>										
CXRMate-RRG24	0.414	0.589	0.493	0.617	0.415	0.563	0.764	0.656	0.577	0.255
MAIRA-2 (w/ grounding)	0.304	0.490	0.442	0.639	0.283	0.397	0.751	0.603	0.496	0.120
MAIRA-2 (w/o grounding)	0.386	0.555	0.425	0.578	0.385	0.534	0.693	0.576	0.501	0.143
MedGemma-4B-IT	0.382	0.547	0.332	0.452	0.494	0.692	0.714	0.580	0.532	0.112
<i>— Specialized Fine-tuning —</i>										
MedGemma-FT (RG only)	0.353	0.520	<u>0.469</u>	0.621	0.323	0.447	0.753	0.624	0.536	<u>0.203</u>
<i>— CURE Inference Strategies (Single Model) —</i>										
CURE (GRG Prompt)	0.314	0.464	0.442	0.606	0.290	0.376	0.725	0.526	0.447	0.077
CURE (AGR-G-9)	0.230	0.443	0.431	0.639	0.225	0.339	0.762	0.608	0.557	0.200
CURE (AGR-G-9 + GRG)	0.355	0.529	0.435	0.601	0.341	0.472	0.784	0.639	0.572	0.200
CURE (AGR-G-29)	0.400	0.559	0.355	0.446	0.540	0.749	0.783	0.645	<u>0.592</u>	0.181
CURE (AGR-G-29 + GRG)	0.415	<u>0.562</u>	0.365	0.439	0.582	<u>0.781</u>	0.792	<u>0.655</u>	0.598	0.176
CURE (AGR-G-38)	0.395	0.534	0.356	0.408	<u>0.594</u>	0.770	<u>0.793</u>	0.632	0.577	0.172
CURE (AGR-G-38 + GRG)	0.406	0.536	0.362	0.404	0.628	0.798	0.800	0.642	0.583	0.169

Table 16. **Anatomical Query Configurations.** Definition of the location sets used for the AGRG inference protocols. **AGR-G-29** represents the set of locations with complete supervision (Bounding Box + Text) in Chest Imagenome. **AGR-G-38** extends this to include locations that have only text supervision. **AGR-G-9** is a subset of core locations.

Config.	Anatomical Locations Included
AGR-G-9	Core Locations: Abdomen, Cardiac Silhouette, Left/Right Costophrenic Angle, Left/Right Lung, Mediastinum, Spine, Trachea.
AGR-G-29	Includes all AGRG-9 plus: Aortic Arch, Carina, Cavaotrial Junction, SVC, Upper Mediastinum, Left/Right Apical Zone, Left/Right Mid Lung Zone, Left/Right Lower Lung Zone, Left/Right Upper Lung Zone, Left/Right Hilar Structures, Left/Right Clavicle, Left/Right Hemidiaphragm, Right Atrium.
AGR-G-38	Includes all AGRG-29 plus: Left/Right Arm, Left/Right Breast, Left/Right Chest Wall, Left/Right Shoulder, Neck.

ing this configuration yields a strong balance of metrics, notably achieving the second-highest RaTEScore (0.592), validating the quality of training on fully grounded data.

- **AGR-G-38 (High Recall):** Expanding to 38 locations includes peripheral areas (e.g., neck, chest wall) that possess text supervision but lack bounding box annotations in the training data. Forcing the model to scrutinize these areas results in the highest Recall (R-Mi **0.770**) and CheXbert Cosine Similarity (**0.793**) among the purely anatomical approaches. However, this exhaustive search introduces a trade-off: while recall improves, precision drops significantly (P-Mi 0.408) compared to the concise AGRG-9 configuration (P-Mi 0.639), leading to slightly

lower aggregate F1 scores compared to the AGRG-29 configuration.

Baseline Performance Analysis. We observe distinct performance profiles across the evaluated baselines. **CXRMate-RRG24** [33] establishes a strong benchmark, achieving the highest RadGraph F1 (**0.255**), CheXbert F1-Micro (**0.589**), and CXRFEScore (**0.656**), reflecting its optimization via reinforcement learning for clinical correctness. For **MAIRA-2**, the inference mode dictates a clear trade-off: the grounded mode maximizes precision (P-Mi **0.639**) but acts as a constraint that limits recall (0.397), whereas disabling grounding improves clinical finding detection (F1-Mi 0.555) but degrades semantic alignment (Cosine drops to 0.693). Finally, comparing the **MedGemma** variants reveals the impact of domain adaptation. The base **MedGemma-4B-IT** exhibits high recall (0.692) but low precision (0.452) and structural accuracy (RadF1 0.112). Surprisingly, fine-tuning solely on reports (**MedGemma-FT (RG)**) resulted in lower CheXbert F1 scores compared to the base model (e.g., F1-Ma 0.353 vs 0.382), although it significantly improved precision to 0.621 and achieved the second-best RadGraph F1 (0.203). However, this specialized baseline still lags behind the multi-task CURE variants in multiple metrics, such as RaTEScore (0.598 vs. 0.536) and Cosine Similarity (0.792 vs. 0.753). This suggests that the explicit grounding tasks in CURE provide a more robust supervision signal for learning to describe radiological findings than standard text-only fine-tuning.

Benefits of Hybrid Inference. The standalone GRG prompt produces concise reports but yields lower recall (R-Mi: 0.376). Combining this global summary with fine-grained anatomical descriptions (**AGR+GRG**) consistently yields the strongest empirical balance in our experiments. Specifically, the **AGR-29 + GRG** configuration achieves the highest **RaTEScore (0.598)** in the table. Furthermore, this configuration achieves a CheXbert F1-Macro of **0.415**, marginally outperforming the state-of-the-art model CXRMate-RRG24 [33] (0.414), the winner of a recent report generation competition. This indicates that fusing a holistic global grounded report with specific, visually grounded regional descriptions is a promising strategy to bridge the gap between precision and recall in radiology report generation.

Additional Comparison with Baselines. CURE demonstrates strong performance against specialized baselines. While **CXRMate-RRG24** [33] retains the top performance on RadGraph F1 (0.255 vs. 0.176), CURE outperforms it on **RaTEScore** (0.598 vs. 0.577) and CheXbert Cosine Similarity (0.792 vs. 0.764). The strong performance on RaTEScore—a recently proposed metric designed to assess medical entities and robustness to synonyms—highlights CURE’s ability to generate clinically relevant content. Furthermore, the hybrid CURE configurations consistently surpass the MAIRA-2 baseline in semantic and factual consistency metrics; specifically, **AGR-29 + GRG** achieves a CXRFEScore of 0.655 (compared to MAIRA-2’s 0.603) and a RaTEScore of 0.598 (compared to MAIRA-2’s 0.496).

9.3. Extended Hallucination Analysis

To provide a holistic view of model reliability, we extend the hallucination analysis from the main paper to the full spectrum of the Chest Imagenome schema. As detailed in the anatomical configurations (Table 16), we focus specifically on the locations for which text supervision is available (typically accompanied by bounding boxes). This selection excludes locations with bounding-box-only supervision, resulting in a comprehensive evaluation set of 38 anatomical regions. Tables 17 and 18 present the performance breakdown across these locations.

Methodology. Unlike the focused analysis in the main paper, this supplementary evaluation covers all 38 anatomical regions present in the training set with text supervision (out of 45 total locations in the schema). For each anatomy, we sampled 300 instances from the test set. To assess MAIRA-2, we utilized its **phrase grounding** capability, prompting the model with the specific anatomical name (e.g., “left clavicle”) to elicit a grounded response using its official

prompt template available at <https://huggingface.co/microsoft/maira-2>.

We employed gemini-2.5-flash-lite as an automated clinical judge to compare the anatomy-specific generation (GEN) against the full ground-truth report (GT). Using a Chain-of-Thought (CoT) prompting strategy, the judge evaluated:

1. **Correctness:** Does GEN successfully retrieve findings present in GT?
2. **Hallucination:** Does GEN invent findings not supported by GT?
3. **NLI Consistency:** What is the logical relationship (Entailment, Contradiction, Neutral) between GEN and GT?

Evaluation Prompt. The exact prompt utilized for the automated judge is provided below. It enforces an independent extraction step before comparison to minimize reasoning errors.

```
You are an expert radiologist. Your task is to compare a short anatomy-specific mini-report [GEN] against a full image ground-truth report [GT], where [GT] was generated by a radiologist over the entire image, whereas [GEN] was generated by a model over a specific anatomical location. You will assess the degree of hallucination and contradiction in [GEN] compared to [GT].
```

First, independently assess each report:

- If [GT] explicitly affirms the presence of any abnormality, set "gt_has_abnormalities" to "yes". Otherwise, set it to "no".
- If [GT] explicitly affirms the presence of any medical device (e.g., pacemaker, catheter, wires), set "gt_has_devices" to "yes". Otherwise, set it to "no".
- If [GEN] explicitly affirms the presence of any abnormality, set "gen_has_abnormalities" to "yes". Otherwise, set it to "no".
- If [GEN] explicitly affirms the presence of any medical device (e.g., pacemaker, catheter, wires), set "gen_has_devices" to "yes". Otherwise, set it to "no".

Next, perform the comparison based on [GT]:

- If [GEN] affirms the presence of an abnormality and this is clearly supported or reasonably suggested by [GT], set "gen_has_correct_abnormalities" to "yes". Otherwise, set it to "no".
- If [GEN] affirms the presence of an abnormality that is NOT affirmed nor supported by [GT], set "gen_has_hallucinated_abnormalities" to "yes". Otherwise, set it to "no".
- If [GEN] affirms the presence of a device that is clearly supported or reasonably suggested by [GT], set "gen_has_correct_devices" to "yes". Otherwise, set it to "no".
- If [GEN] affirms the presence of a device that is NOT affirmed nor supported by [GT], set "gen_has_hallucinated_devices" to "yes". Otherwise, set it to "no".
- Natural Language Inference:
 - If [GEN] makes at least one explicit statement that is clearly contradicted by [GT], set "nli_status" to "contradiction".
 - If all of [GEN]’s explicit statements are reasonably supported by [GT], set "nli_status" to "entailment".
 - Otherwise, set "nli_status" to "neutral".

```

You must respond ONLY with a single, valid JSON object
in the following format. Do not add any text
before or after the JSON object.

{
  "reason": "A detailed explanation of your reasoning
  for the comparison. Include a brief explanation
  of why you made your choices for each field.
  Focus on what is explicitly stated in [GEN] and
  [GT]. Do not make any assumptions about what is
  not explicitly stated.",
  "gt_has_abnormalities": "yes" | "no",
  "gt_has_devices": "yes" | "no",
  "gen_has_abnormalities": "yes" | "no",
  "gen_has_devices": "yes" | "no",
  "gen_has_correct_abnormalities": "yes" | "no",
  "gen_has_hallucinated_abnormalities": "yes" | "no",
  "gen_has_correct_devices": "yes" | "no",
  "gen_has_hallucinated_devices": "yes" | "no",
  "nli_status": "contradiction" | "entailment" |
    "neutral"
}

```

Results and Analysis. The comprehensive breakdown in Tables 17 and 18 highlights distinct behavioral profiles:

- **MAIRA-2 and NLI Neutrality:** MAIRA-2 exhibits a notably high *Neutral* NLI rate (73.2%) and low Abnormality Correctness (3.6%). This is the behavior one would generally expect from MAIRA-2’s phrase grounding formulation: when prompted with an anatomical phrase, the model frequently outputs the phrase verbatim with coordinates, without adding descriptive adjectives. Since the output merely identifies the anatomy without making a clinical claim, the NLI judge correctly labels the relationship to the ground truth as *Neutral*. However, we observe that MAIRA-2 does occasionally append additional descriptions. When this occurs, it is highly prone to hallucination (14.9% rate), suggesting that deviations from the standard localization behavior often result in factual errors rather than useful clinical insights.
- **Sensitivity-Specificity Trade-off:** CURE demonstrates a favorable shift in the trade-off between Sensitivity (the ability to correctly identify abnormalities) and Specificity (the ability to avoid false positives). In this context, we associate *Abnormality Correctness* with Sensitivity and *Hallucination Rate* with the inverse of Specificity. CURE maintains a hallucination rate comparable to MAIRA-2 (15.2% vs. 14.9%) while achieving a massive improvement in Correctness (17.8% vs 3.6%, an approximately 5× increase). This indicates that CURE’s generations are more clinically useful and aligned with radiologist findings (Entailment: 43.2% vs. 9.3%), rather than defaulting to the “safe silence” of simple object localization.
- **Anatomical Specificity:** CURE demonstrates remarkable robustness on structures where MAIRA-2 fails. For instance, on the **Left and Right Clavicles**, MAIRA-2’s attempts to describe the region result in hallucination rates of 59.0% and 62.7%, respectively. This likely reflects a bias in MAIRA-2’s training distribution, where

mentions of the clavicles were presumably highly correlated with fractures, leading the model to hallucinate pathology even when performing a grounding task. In contrast, CURE reduces this hallucination rate to 1.0% in both cases.

- **Device Recognition:** CURE significantly outperforms MAIRA-2 in identifying medical devices (**14.0%** Correctness vs. 1.3%). It is important to note that MAIRA-2’s low performance here is largely a consequence of the task formulation. MAIRA-2 is designed for specific tasks, and when performing phrase grounding using the standard prompt, it effectively localizes the structure but does not spontaneously describe the presence of devices (e.g., catheters). It is not designed as a flexible instruction-following model that can be prompted to exhaustively list findings. CURE, conversely, is trained on the AGRG objective to inherently describe the contents of the anatomical region, leading to stronger detection rates in device-heavy regions like the *Cavoatrial Junction* (45.3% Correctness).

Qualitative Example. Table 19 provides a concrete instance of the evaluation protocol applied to the *Left Clavicle*, validating the statistical trends observed above. In this scenario, the ground truth explicitly affirms that “Bony structures are intact.” MAIRA-2, reflecting the high hallucination bias observed for this anatomy ($\approx 60\%$), generates a specific but incorrect finding: “Left clavicle fracture is noted.” The automated judge correctly identifies this incompatibility, marking it as a *Contradiction* and a *Hallucination*. In contrast, CURE correctly generates a negative finding (“No acute osseous abnormalities”), which the judge recognizes as supported by the ground truth (*Entailment*). This example illustrates the robustness of the automated judge in discerning clinical nuances and highlights the tangible quality improvement achieved by CURE in avoiding specific anatomical hallucinations.

10. Additional Qualitative Analysis

To provide further insight into model behavior, this section includes additional qualitative examples from both the Grounded Report Generation (GRG) and Anatomy Grounded Report Generation (AGRG) tasks.

Grounded Report Generation on VinDr-CXR. Figure 6 presents two additional test samples from the VinDr-CXR dataset. These examples highlight the difficulty of generating reports for complex cases with dense annotations. In these specific instances, both models capture salient clinical features, though challenges remain in fully recovering all localized findings present in the ground truth. Quantitative metrics for these samples remain comparable, with CURE showing a slight advantage in semantic similar-

ity (CheXbert Cosine) and localization (IoU) in both examples.

Anatomy Grounded Report Generation on MIMIC-CXR. Figure 7 displays four examples of anatomy-specific generation. In this task, the model is prompted to locate and describe a specific region. The qualitative results highlight differences in robustness against hallucinations. For instance, in the second row (Left Clavicle), MAIRA-2 incorrectly predicts a fracture. In contrast, CURE accurately focuses its description on the placement of the endotracheal tube—which is the primary finding in the ground truth—avoiding the fracture hallucination and achieving significantly better localization (IoU 0.627 vs 0.206).

Table 17. **Per-anatomy comparison of MAIRA-2 and CURE performance on the Chest ImaGenome subset (Part 1/2).** Each anatomical region reports hallucination and correctness rates (%) for abnormalities and medical devices, along with Natural Language Inference (NLI) consistency metrics: Contradiction (Cont.) and Entailment (Ent.). Lower hallucination and contradiction values, together with higher correctness and entailment, indicate greater clinical agreement between the generated and ground-truth reports. See Table 18 for continuation.

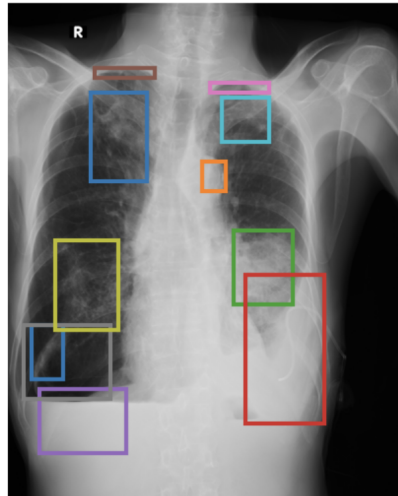
Anatomy	Model	Abn. Halluc. ↓	Abn. Corr. ↑	Dev. Halluc. ↓	Dev. Corr. ↑	Contra. ↓	Entail. ↑	Neutral	N
Abdomen	MAIRA-2	24.0%	6.0%	3.0%	0.7%	35.7%	16.3%	48.0%	300
	CURE	2.0%	1.7%	14.3%	33.0%	9.0%	54.3%	36.7%	300
Aortic Arch	MAIRA-2	1.3%	0.3%	0.0%	0.0%	0.3%	16.3%	83.3%	300
	CURE	64.7%	26.3%	2.0%	1.7%	6.3%	26.0%	67.7%	300
Cardiac Silhouette	MAIRA-2	2.0%	2.7%	0.0%	0.3%	8.0%	25.0%	67.0%	300
	CURE	25.7%	26.3%	1.0%	6.3%	27.7%	47.3%	25.0%	300
Carina	MAIRA-2	0.0%	1.0%	0.0%	0.0%	1.0%	5.7%	93.3%	300
	CURE	6.0%	2.3%	41.0%	14.7%	34.0%	11.0%	55.0%	300
Cavoatrial Junction	MAIRA-2	0.0%	0.0%	0.0%	0.3%	0.3%	12.3%	87.3%	300
	CURE	6.3%	5.7%	32.3%	45.3%	15.0%	47.0%	38.0%	300
Left Apical Zone	MAIRA-2	7.0%	2.0%	0.0%	0.7%	3.7%	3.7%	92.7%	300
	CURE	2.0%	10.3%	0.0%	4.0%	14.0%	61.0%	25.0%	300
Left Arm	MAIRA-2	21.3%	2.0%	0.7%	0.7%	13.3%	6.7%	80.0%	300
	CURE	12.7%	18.7%	1.7%	7.7%	23.7%	42.7%	33.7%	300
Left Breast	MAIRA-2	27.0%	3.7%	1.3%	0.7%	13.7%	6.0%	80.3%	300
	CURE	10.3%	20.0%	1.3%	7.7%	21.0%	44.3%	34.7%	300
Left Chest Wall	MAIRA-2	19.3%	4.7%	11.0%	8.3%	40.0%	9.3%	50.7%	300
	CURE	4.3%	18.0%	5.3%	28.0%	11.7%	68.3%	20.0%	300
Left Clavicle	MAIRA-2	59.0%	2.3%	0.0%	0.3%	22.7%	5.0%	72.3%	300
	CURE	1.0%	4.3%	8.3%	11.3%	7.0%	32.7%	60.3%	300
Left Costophrenic Angle	MAIRA-2	2.0%	1.0%	0.0%	0.0%	2.0%	1.3%	96.7%	300
	CURE	9.3%	18.7%	0.0%	2.0%	26.3%	53.7%	20.0%	300
Left Hemidiaphragm	MAIRA-2	0.7%	0.7%	0.0%	0.0%	0.3%	4.3%	95.3%	300
	CURE	11.7%	9.0%	8.0%	23.3%	6.0%	33.7%	60.3%	300
Left Hilar Structures	MAIRA-2	17.7%	2.7%	0.0%	0.7%	6.3%	5.0%	88.7%	300
	CURE	9.7%	31.3%	0.0%	1.3%	28.3%	52.3%	19.3%	300
Left Lower Lung Zone	MAIRA-2	11.7%	10.0%	0.0%	0.0%	8.3%	11.7%	80.0%	300
	CURE	25.3%	40.0%	0.0%	5.7%	17.3%	53.0%	29.7%	300
Left Lung	MAIRA-2	12.0%	9.3%	0.3%	3.0%	56.3%	21.7%	22.0%	300
	CURE	7.0%	12.0%	0.0%	3.3%	32.3%	41.7%	26.0%	300
Left Mid Lung Zone	MAIRA-2	11.0%	4.7%	0.0%	0.0%	4.7%	4.3%	91.0%	300
	CURE	61.0%	37.7%	0.0%	2.7%	40.3%	29.3%	30.3%	300
Left Shoulder	MAIRA-2	31.3%	2.7%	1.3%	0.3%	15.7%	4.7%	79.7%	300
	CURE	10.3%	20.0%	5.7%	8.0%	22.7%	44.0%	33.3%	300
Left Upper Lung Zone	MAIRA-2	15.3%	8.3%	0.0%	0.0%	8.0%	7.3%	84.7%	300
	CURE	38.7%	38.3%	0.0%	2.3%	15.7%	38.3%	46.0%	300
Mediastinum	MAIRA-2	23.7%	14.3%	0.0%	4.3%	67.0%	14.0%	19.0%	300
	CURE	5.3%	6.0%	12.3%	33.7%	20.7%	49.7%	29.7%	300

Table 18. **Per-anatomy comparison of MAIRA-2 and CURE performance on the Chest Imagenome subset (Part 2/2).** Continuation of Table 17. Each row corresponds to an anatomical region evaluated for abnormality and device hallucination (%) and correctness (%), as well as NLI-based Contradiction (Cont.) and Entailment (Ent.) rates. Lower hallucination and contradiction, and higher correctness and entailment, reflect more clinically faithful and factually consistent report generation.

Anatomy	Model	Abn. Halluc. ↓	Abn. Corr. ↑	Dev. Halluc. ↓	Dev. Corr. ↑	Contra. ↓	Entail. ↑	Neutral	N
Neck	MAIRA-2	17.0%	3.7%	2.7%	1.7%	58.3%	4.3%	37.3%	300
	CURE	1.0%	2.0%	27.0%	62.0%	20.7%	41.7%	37.7%	300
Right Apical Zone	MAIRA-2	7.3%	3.7%	0.0%	2.0%	5.7%	6.3%	88.0%	300
	CURE	6.3%	13.0%	0.0%	8.0%	20.0%	54.0%	26.0%	300
Right Arm	MAIRA-2	21.7%	2.0%	1.7%	1.0%	16.3%	5.3%	78.3%	300
	CURE	7.0%	16.3%	2.3%	5.3%	23.0%	40.0%	37.0%	300
Right Atrium	MAIRA-2	0.7%	0.3%	0.0%	0.3%	1.0%	11.3%	87.7%	300
	CURE	8.3%	3.3%	37.0%	45.3%	12.3%	39.7%	48.0%	300
Right Breast	MAIRA-2	21.0%	1.0%	1.3%	1.0%	11.3%	5.7%	83.0%	300
	CURE	9.7%	19.3%	3.0%	4.7%	22.0%	41.3%	36.7%	300
Right Chest Wall	MAIRA-2	23.0%	6.0%	5.0%	3.7%	39.7%	10.7%	49.7%	300
	CURE	2.0%	23.7%	6.0%	20.0%	12.7%	67.0%	20.3%	300
Right Clavicle	MAIRA-2	62.7%	0.3%	0.0%	0.7%	20.3%	1.7%	78.0%	300
	CURE	1.0%	4.3%	4.3%	8.7%	7.3%	27.7%	65.0%	300
Right Costophrenic Angle	MAIRA-2	1.3%	4.7%	0.0%	0.3%	0.3%	5.7%	94.0%	300
	CURE	10.7%	25.0%	0.3%	3.3%	25.3%	49.0%	25.7%	300
Right Hemidiaphragm	MAIRA-2	0.7%	0.0%	0.0%	0.0%	0.0%	6.3%	93.7%	300
	CURE	8.7%	8.7%	7.3%	21.7%	8.7%	45.3%	46.0%	300
Right Hilar Structures	MAIRA-2	17.0%	2.7%	0.0%	0.7%	7.0%	6.3%	86.7%	300
	CURE	13.0%	32.3%	0.0%	2.3%	31.3%	49.0%	19.7%	300
Right Lower Lung Zone	MAIRA-2	8.0%	5.3%	0.0%	0.0%	6.0%	5.3%	88.7%	300
	CURE	25.3%	43.7%	0.0%	4.0%	18.7%	53.3%	28.0%	300
Right Lung	MAIRA-2	10.7%	9.7%	0.0%	3.0%	53.7%	29.3%	17.0%	300
	CURE	11.7%	21.3%	0.3%	7.3%	27.0%	46.0%	27.0%	300
Right Mid Lung Zone	MAIRA-2	8.7%	2.0%	0.0%	0.0%	6.0%	2.3%	91.7%	300
	CURE	66.0%	33.0%	0.0%	2.7%	43.3%	23.0%	33.7%	300
Right Shoulder	MAIRA-2	32.0%	1.3%	0.7%	0.0%	16.3%	4.7%	79.0%	300
	CURE	8.7%	22.7%	10.0%	16.3%	23.7%	45.3%	31.0%	300
Right Upper Lung Zone	MAIRA-2	9.7%	3.0%	0.0%	0.0%	6.3%	3.3%	90.3%	300
	CURE	47.0%	36.0%	0.0%	4.0%	24.7%	31.7%	43.7%	300
Spine	MAIRA-2	12.7%	6.0%	5.7%	4.7%	38.3%	13.0%	48.7%	300
	CURE	6.3%	11.7%	0.7%	2.7%	3.3%	41.7%	55.0%	300
SVC	MAIRA-2	9.3%	1.0%	4.0%	5.0%	11.0%	19.0%	70.0%	300
	CURE	5.7%	1.7%	34.3%	42.0%	17.7%	34.7%	47.7%	300
Trachea	MAIRA-2	7.7%	0.3%	0.0%	0.0%	26.3%	16.0%	57.7%	300
	CURE	19.3%	2.0%	21.0%	21.7%	24.3%	19.7%	56.0%	300
Upper Mediastinum	MAIRA-2	10.0%	5.7%	0.3%	4.0%	33.0%	16.3%	50.7%	300
	CURE	7.7%	10.7%	4.3%	8.7%	21.7%	61.0%	17.3%	300
Mean	MAIRA-2	14.9%	3.6%	1.0%	1.3%	17.5%	9.3%	73.2%	300
Mean	CURE	15.2%	17.8%	7.7%	14.0%	20.2%	43.2%	36.6%	300

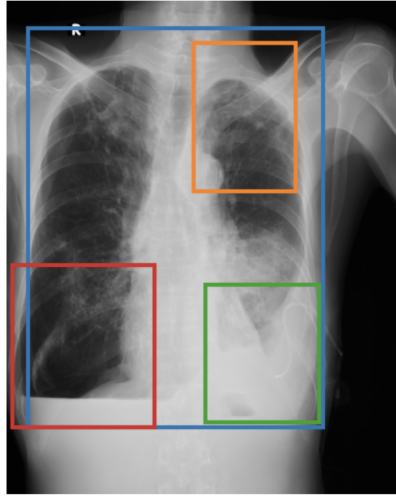
Table 19. **Qualitative Example of the Automated Evaluation Protocol.** We employ `gemini-2.5-flash-lite` to perform detailed hallucination and Natural Language Inference (NLI) analysis, utilizing the prompt defined in Section 9.3. This case illustrates the evaluation for the *Left Clavicle*. The automated judge compares the model-generated anatomy-specific report (GEN) against the full ground-truth report (GT). MAIRA-2 hallucinates a fracture, leading to a *Contradiction*, whereas CURE correctly identifies the lack of abnormalities, resulting in *Entailment*.

 <p>Context: Ground Truth (GT) Report "AP upright portable chest radiograph is obtained. A left chest wall pacer device is again seen with lead tips extending into the right atrium and ventricle. Abandoned pacing leads are also seen in the right chest wall, extending into the right heart, not significantly changed. The heart is mildly enlarged. The lungs appear clear without definite signs of pneumonia or CHF. No large effusion or pneumothorax is seen. The overall cardiomeastinal silhouette is stable. Bony structures are intact. No acute findings in the chest. Stable mild cardiomegaly. Multiple pacer wires are unchanged in position."</p>	
Target Anatomy: Left Clavicle	
Model	Generated Output & Gemini 2.5 Flash-Lite's Evaluation
MAIRA-2	<p>Generation: Left clavicle fracture is noted. [0.645, 0.145, 0.995, 0.345]</p> <p>Gemini 2.5 Flash-Lite's Evaluation: { "reason": "The Ground Truth ([GT]) report describes a left chest wall pacer device, abandoned pacing leads in the right chest wall, mild cardiomegaly, and stable findings, but it explicitly states that 'Bony structures are intact' and 'No acute findings in the chest.' The Mini-Report ([GEN]) states 'Left clavicle fracture is noted.' Since the GT explicitly states bony structures are intact and no acute findings are seen, the mention of a left clavicle fracture in [GEN] is a clear contradiction to the findings in [GT].\n - gt_has_abnormalities: Yes, due to mild cardiomegaly.\n - gt_has_devices: Yes, due to the presence of pacer devices and leads.\n - gen_has_abnormalities: Yes, a fracture is an abnormality.\n - gen_has_devices: No devices are mentioned in [GEN].\n - gen_has_correct_abnormalities: No, the fracture is not supported; in fact, bony structures are reported as intact.\n - gen_has_hallucinated_abnormalities: Yes, the fracture is not mentioned in [GT] and contradicts the statement that bony structures are intact.\n - gen_has_correct_devices: No, [GEN] does not mention devices.\n - gen_has_hallucinated_devices: No, [GEN] does not mention devices.\n - nli_status: Contradiction, because [GEN] reports a fracture while [GT] reports bony structures as intact and no acute findings.", "gt_has_abnormalities": "yes", "gt_has_devices": "yes", "gen_has_abnormalities": "yes", "gen_has_devices": "no", "gen_has_correct_abnormalities": "no", "gen_has_hallucinated_abnormalities": "yes", "gen_has_correct_devices": "no", "gen_has_hallucinated_devices": "no", "nli_status": "contradiction" }</p>
CURE	<p>Generation: Location of the left clavicle: [0.75,0.28,0.36,0.19]. Description: No acute osseous abnormalities.</p> <p>Gemini 2.5 Flash-Lite's Evaluation: { "reason": "The ground truth report [GT] states, \"Bony structures are intact\" and \"No acute findings in the chest,\" which implies no acute osseous abnormalities. The mini-report [GEN] states, \"No acute osseous abnormalities.\" This statement is directly supported by [GT].\n - [GT] mentions a pacer device and leads, so gt_has_devices is 'yes'. It mentions mild cardiomegaly, so gt_has_abnormalities is 'yes'.\n - [GEN] mentions no abnormalities, so gen_has_abnormalities is 'no'. [GEN] mentions no devices, so gen_has_devices is 'no'.\n - [GEN] does not affirm any abnormality, so gen_has_correct_abnormalities and gen_has_hallucinated_abnormalities are 'no'.\n - [GEN] does not affirm any device, so gen_has_correct_devices and gen_has_hallucinated_devices are 'no'.\n - Since the statement in [GEN] (\"No acute osseous abnormalities\") is directly supported by the statement in [GT] (\"Bony structures are intact\"), the NLI status is 'entailment'.", "gt_has_abnormalities": "yes", "gt_has_devices": "yes", "gen_has_abnormalities": "no", "gen_has_devices": "no", "gen_has_correct_abnormalities": "no", "gen_has_hallucinated_abnormalities": "no", "gen_has_correct_devices": "no", "gen_has_hallucinated_devices": "no", "nli_status": "entailment" }</p>



(a) Ground Truth

Atelectasis [0.06, 0.65, 0.14, 0.76]. Calcification [0.49, 0.32, 0.55, 0.38]. Consolidation [0.57, 0.46, 0.72, 0.61]. Pleural effusion [0.60, 0.55, 0.80, 0.85] [0.08, 0.78, 0.30, 0.91]. Pleural thickening [0.22, 0.13, 0.37, 0.15] [0.51, 0.16, 0.66, 0.18]. Pneumothorax [0.04, 0.65, 0.26, 0.80]. Pulmonary fibrosis [0.12, 0.48, 0.28, 0.66] [0.54, 0.19, 0.66, 0.28] [0.21, 0.18, 0.35, 0.36]. Tuberculosis. Other diseases.

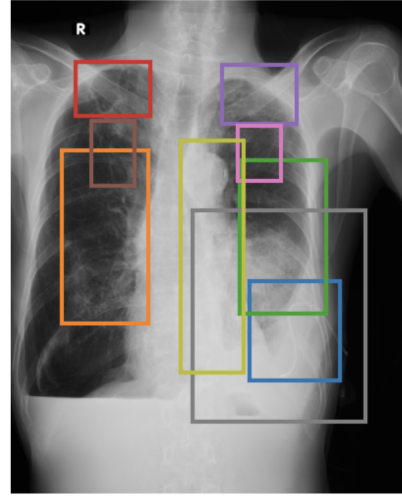


(b) MAIRA-2

The heart size is normal. Lung fields are hyperaerated bilaterally. [0.055, 0.055, 0.805, 0.865] There is pleural calcification in the left upper lobe. [0.475, 0.085, 0.735, 0.385] There is blunting of the left cp angle. [0.505, 0.575, 0.795, 0.855] There is pleural calcification in the right lower hemithorax. [0.015, 0.535, 0.375, 0.865] There is blunting of the right cp angle.

Metrics:

IoU: 0.311
CheXbert Cos: 0.767
CheXbert Acc: 0.571
CXRFEScore: 0.416

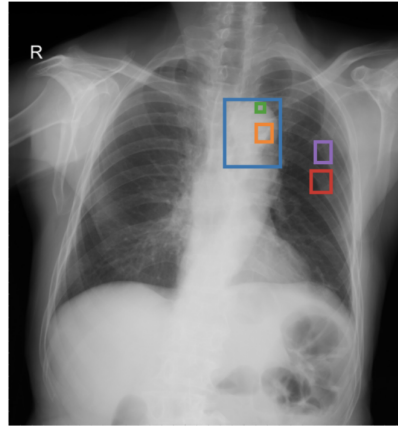


(c) CURE

Left pleural effusion without significant changes [0.72, 0.67, 0.23, 0.20]. Chronic changes in the lung parenchyma [0.24, 0.48, 0.22, 0.35] [0.69, 0.48, 0.22, 0.31]. Biapical pleuroparenchymal thickening [0.26, 0.18, 0.19, 0.11] [0.63, 0.19, 0.19, 0.12]. Calcified granulomas [0.26, 0.31, 0.11, 0.13] [0.63, 0.31, 0.11, 0.11]. Changes from left mastectomy [0.68, 0.64, 0.44, 0.43]. Aortic elongation [0.51, 0.52, 0.16, 0.47]

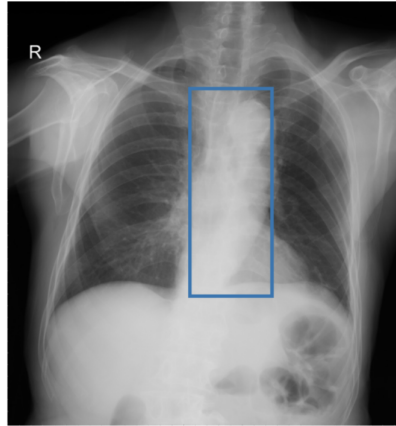
Metrics:

IoU: 0.320
CheXbert Cos: 0.834
CheXbert Acc: 0.643
CXRFEScore: 0.523



(d) Ground Truth

Aortic enlargement [0.55, 0.23, 0.69, 0.39]. Calcification [0.63, 0.29, 0.67, 0.33] [0.63, 0.24, 0.65, 0.26]. Rib fracture [0.77, 0.40, 0.82, 0.45] [0.78, 0.33, 0.82, 0.38]. Other diseases.

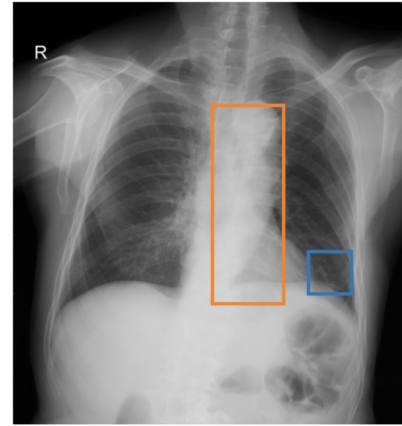


(e) MAIRA-2

Normal cardiac silhouette. The lung fields are clear. No evidence of hilar adenopathy. No evidence of mediastinal adenopathy. Skeletal structures are unremarkable. The aorta is tortuous. [0.465, 0.205, 0.675, 0.695]

Metrics:

IoU: 0.182
CheXbert Cos: 0.738
CheXbert Acc: 0.786
CXRFEScore: 0.316



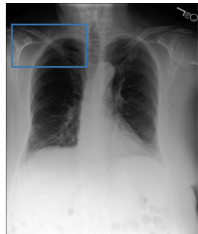
(f) CURE

Left basal laminar atelectasis [0.81, 0.64, 0.11, 0.10]. Aortic elongation [0.60, 0.48, 0.18, 0.47]. No other relevant findings

Metrics:

IoU: 0.199
CheXbert Cos: 0.755
CheXbert Acc: 0.786
CXRFEScore: 0.350

Figure 6. Qualitative comparison of two examples of grounded report generation (GRG) from the **VinDr-CXR** dataset. The **top row** (**a-c**) shows the first example, and the **bottom row** (**d-f**) shows the second example. For each, the left column represents ground-truth annotations, the middle is MAIRA-2, and the right is CURE. The colored coordinates in the text correspond to bounding boxes drawn in the images. Per-sample metrics are provided below the predicted reports.

(a) Ground Truth

Loc: Right Clavicle
Osseous structures are diffusely demineralized.
[0.03, 0.09, 0.42, 0.28]

(b) MAIRA-2

Right clavicle is fractured.
[0.07, 0.01, 0.28, 0.14]

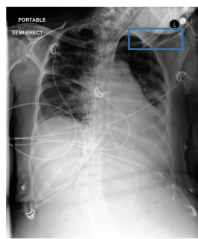
Metrics:
IoU: 0.097
CheXbert Cos: 0.459
CheXbert Acc: 0.857
CXRFEscore: 0.119

(c) CURE

Location of the right clavicle:
[0.22, 0.21, 0.39, 0.12].

Description: No acute osseous abnormalities.

Metrics:
IoU: 0.643
CheXbert Cos: 0.882
CheXbert Acc: 1.000
CXRFEscore: 0.513

(d) Ground Truth

Loc: Left Clavicle
ETT tip at clavicle margin.
No bone abnormalities.
[0.64, 0.09, 0.92, 0.18]

(e) MAIRA-2

Left clavicle fracture. [0.69, 0.01, 0.93, 0.14]

Metrics:
IoU: 0.206
CheXbert Cos: 0.303
CheXbert Acc: 0.786
CXRFEscore: 0.404

(f) CURE

Location of the left clavicle:
[0.75, 0.14, 0.26, 0.12].

Description: The patient is intubated, the ETT terminating in the trachea 4 cm above the level of the carina.

Metrics:
IoU: 0.627
CheXbert Cos: 0.880
CheXbert Acc: 1.000
CXRFEscore: 0.467

(g) Ground Truth

Loc: Right Lung
There is a diffuse mild interstitial abnormality in the right lung, unchanged from prior. There is no evidence of consolidation or edema.
There is no pleural effusion or pneumothorax. There is evidence of stable pulmonary hypertension and vascular engorgement. [0.086, 0.219, 0.466, 0.705]

(h) MAIRA-2

Right lung is clear.

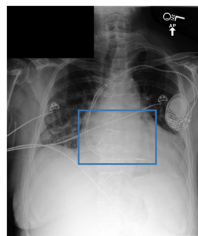
Metrics:
IoU: 0.000
CheXbert Cos: 0.716
CheXbert Acc: 0.929
CXRFEscore: 0.530

(i) CURE

Location of the right lung:
[0.28, 0.48, 0.36, 0.48].

Description: There is mild pulmonary vascular congestion. No pleural effusion or pneumothorax is seen. Mild pulmonary vascular congestion.

Metrics:
IoU: 0.879
CheXbert Cos: 0.699
CheXbert Acc: 0.929
CXRFEscore: 0.805

(j) Ground Truth

Loc: Cardiac Silhouette
Moderate cardiomegaly is unchanged. A left-sided dual-chamber pacemaker is present with leads in the right atrium and right ventricle.
[0.375, 0.451, 0.778, 0.683]

(k) MAIRA-2

cardiac silhouette. [0.37, 0.47, 0.93, 0.84]

Metrics:
IoU: 0.411
CheXbert Cos: 0.723
CheXbert Acc: 0.929
CXRFEscore: 0.515

(l) CURE

Location of the cardiac silhouette:
[0.61, 0.59, 0.51, 0.26].

Description: FINDINGS: In comparison with the study of ..., there is continued enlargement of the cardiac silhouette with a dual-channel pacer device in place.

Metrics:
IoU: 0.657
CheXbert Cos: 0.725
CheXbert Acc: 0.929
CXRFEscore: 0.659

Figure 7. Qualitative comparison of Anatomy Grounded Report Generation (AGR) on the **MIMIC-CXR** test set. We display images and reports side-by-side for compactness. Rows correspond to: **(a-c)** Right Clavicle, **(d-f)** Left Clavicle, **(g-i)** Right Lung, and **(j-l)** Cardiac Silhouette. The left block is ground-truth, middle is MAIRA-2, and right is CURE. Per-sample metrics are provided below each anatomy-grounded report.